

Universal control and error correction in multi-qubit spin registers in diamond

T. H. Taminiau¹, J. Cramer¹, T. van der Sar¹, V. V. Dobrovitski², and R. Hanson¹

¹*Kavli Institute of Nanoscience, Delft University of Technology,
PO Box 5046, 2600 GA Delft, The Netherlands.*

²*Ames Laboratory and Iowa State University, Ames, Iowa 50011, USA.*

Quantum registers of nuclear spins coupled to electron spins of individual solid-state defects are a promising platform for quantum information processing [1-13]. Pioneering experiments selected defects with favourably located nuclear spins having particularly strong hyperfine couplings [4-10]. For progress towards large-scale applications, larger and deterministically available nuclear registers are highly desirable. Here we realize universal control over multi-qubit spin registers by harnessing abundant weakly coupled nuclear spins. We use the electron spin of a nitrogen-vacancy centre in diamond to selectively initialize, control and read out carbon-13 spins in the surrounding spin bath and construct high-fidelity single- and two-qubit gates. We exploit these new capabilities to implement a three-qubit quantum-error-correction protocol [14-17] and demonstrate the robustness of the encoded state against applied errors. These results transform weakly coupled nuclear spins from a source of decoherence into a reliable resource, paving the way towards extended quantum networks and surface-code quantum computing based on multi-qubit nodes [11,18,19].

Electron and nuclear spins associated with defects in solids provide natural hybrid quantum registers [3-11]. Fully-controlled registers of multiple spins hold great promise as building blocks for quantum networks [18] and fault-tolerant quantum computing [19]. The defect electron spin enables initialization and readout of the register and coupling to other (distant) electron spins [11,18], whereas the nuclear spins provide well-isolated qubits and memories with long coherence times [8,9,11]. Previous experiments relied on selected defects having nuclear spins with strong hyperfine couplings that exceed the inverse of the electron spin dephasing time ($1/T_2^*$). With these strongly coupled spins, single-shot readout [9,10,20-22] and entanglement [9,11] were demonstrated. However, the number of strongly coupled spins varies per defect and is intrinsically limited, so that universal control has so far been restricted to two-qubit registers [4,7] and the required control of multi-qubit registers has remained an open challenge.

Here we overcome this challenge by demonstrating universal control of weakly coupled nuclear spins (unresolved hyperfine coupling $1/T_2^*$). We use the electron spin of single nitrogen-vacancy (NV) centres in room-temperature diamond to selectively control multiple carbon-13 (^{13}C) nuclear spins in the surrounding spin bath (Fig. 1a). With this new level of control we realize multi-qubit registers by constructing high-fidelity unconditional and electron-controlled gates, implementing initialization and readout, and creating nuclear-nuclear entangling gates through the electron spin. Finally, we demonstrate the power of this approach by implementing the first quantum-error-correction protocol with individual solid-state spins.

We have used dynamical decoupling spectroscopy [23-25] to characterize the nuclear spin environment of a total of three NV centres, including one with an additional strongly coupled ^{13}C spin (Supplementary Information). To demonstrate the universality of our approach to create multi-qubit registers, we have realized initialization, control and readout of three weakly coupled ^{13}C spins for each NV centre studied (Supplementary Information). Below we consider one of these NV centres in detail and use two of its weakly coupled ^{13}C spins to form a three-qubit register for quantum error correction (Fig. 1a).

Our control method exploits the dependence of the nuclear spin quantization axis on the electron spin state due to the anisotropic hyperfine interaction (see Methods for hyperfine parameters), so that no radio-frequency driving of the nuclear spins is required [23-27]. All nuclear gates are implemented by pulse sequences of the form $(\tau - \pi - 2\tau - \pi - \tau)^{N/2}$ where π is a microwave pi-pulse on the electron spin, 2τ is the inter-pulse delay and N is the total number of pulses in the sequence. Each nuclear spin is controlled by precisely choosing τ in resonance with that spin's particular hyperfine interaction. The target spin, the type of gate (conditional or unconditional) and the rotation axis (X - or Z -rotation) are determined by the value of τ ; the total rotation angle is determined by N (Methods). Crucially, these sequences at the same time decouple the electron from the other nuclear qubits and the environment [7]; these decoherence-protected gates are selective and allow the full electron coherence time T_{coh} to be exploited ($T_{coh} = 2.86(4)$ ms, Fig. 1b). The gates are thus not limited by the electron spin dephasing time $T_2^* = 3.3(1)$ μs or Hahn echo time T_2 and do not require strong coupling.

To initialize the nuclear spins we first prepare the electron spin in $m_s = 0$ by optical pumping (Supplementary Information), then swap the electron state onto the nuclear spin, and finally re-initialize the electron spin (Fig. 1c). We characterize the nuclear initialization by preparing the electron spin in a superposition state and letting it evolve in a Ramsey-type experiment. Without initialization a single-frequency oscillation with a Gaussian decaying envelope

FIGURE 1

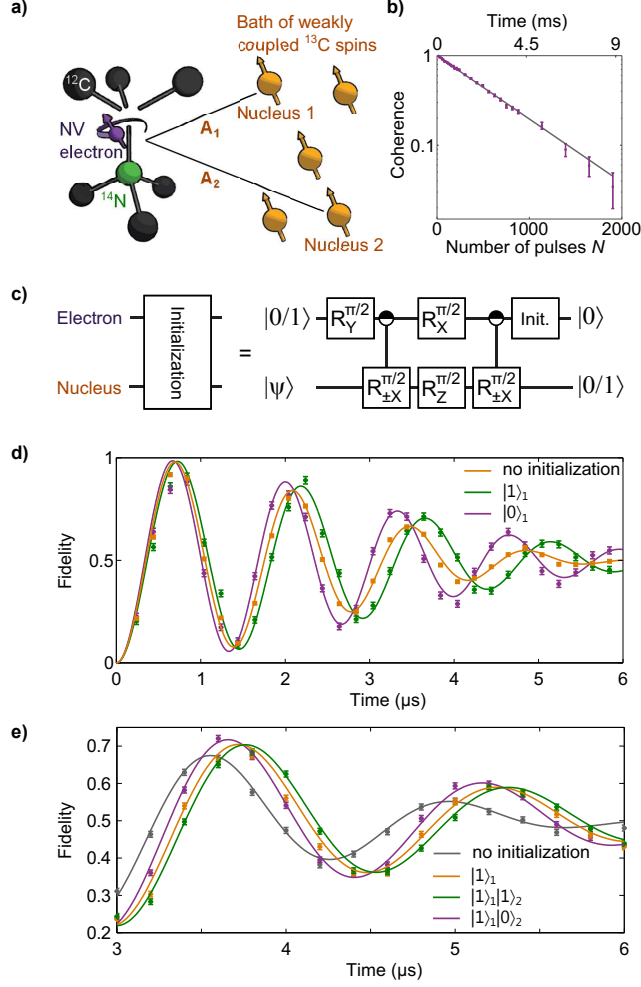


Figure 1: Definition and initialization of the quantum registers. (a) Quantum register formed by the nitrogen-vacancy (NV) electron spin ($S = 1$; $|0\rangle = |m_s = 0\rangle, |1\rangle = |m_s = -1\rangle$) and weakly coupled ^{13}C nuclear spins ($I = 1/2$; state $|\psi\rangle_i$ and hyperfine interaction A_i for nuclear spin i , see Methods for values). All gates on nuclear spins are implemented by sequences of N pi-pulses on the electron spin spaced by a time 2τ (Methods). (b) The electronic coherence as a function of the total sequence length. The number of pi-pulses N is increased for fixed $\tau = 2\pi/\omega_L$, which is representative for our gates.

$\omega_L = 2\pi \cdot 431$ kHz is the ^{13}C Larmor frequency. The $1/e$ time is $T_{coh} = 2.86(4)$ ms. (c) Nuclear spin initialization by swapping the electron state, $|0/1\rangle = |0\rangle$ or $|1\rangle$, onto the nuclear spin. The controlled gates ($R_{\pm X}^{\pi/2}$) are X -rotations by $\pi/2$ with a direction conditional on the electron spin state (Methods). The final electron spin re-initialization by a $2\ \mu\text{s}$ laser pulse (labelled “Init.”) preserves the nuclear spin polarization (T_1 values under illumination: $2.5(3)$ ms for nuclear spin 1 and $1.2(2)$ ms for nuclear spin 2, Supplementary Information). (d) Electron Ramsey measurements without nuclear spin initialization and with nuclear spin 1 initialized in $|0\rangle_1$ or $|1\rangle_1$, and (e) with nuclear spin 1 initialized in $|1\rangle_1$ and nuclear spin 2 in $|0\rangle_2$ or $|1\rangle_2$. All error bars and uncertainties in this work are 1σ .

is observed, confirming that the NV centre feels a decohering bath of weakly coupled spins (Fig. 1d). Initializing one of the nuclear spins in the $|0\rangle$ ($|1\rangle$) state (Fig. 1d and 1e), we increase (decrease) the oscillation frequency because the magnetic field at the electron is enhanced (reduced) due to the hyperfine interaction. The oscillations also persist longer as quasistatic fluctuations of the two nuclear spins are suppressed [28], increasing the electronic dephasing time to $T_2^* = 4.0(2)\ \mu\text{s}$. From this data, we obtain state initialization fidelities of $F_1 = 0.91(2)$ and $F_2 = 0.88(5)$ for nuclear spin 1 and 2 respectively (see Methods).

Next we demonstrate the measurement of the individual nuclear spin states and verify that we observe two distinct ^{13}C spins by performing nuclear free-evolution experiments (Fig. 2a-d). The oscillations in the expectation values $\langle X \rangle$ and $\langle Y \rangle$ show that the nuclear spins states are successfully read out. The precession frequencies, $\omega = 2\pi \cdot 470(1)$

FIGURE 2

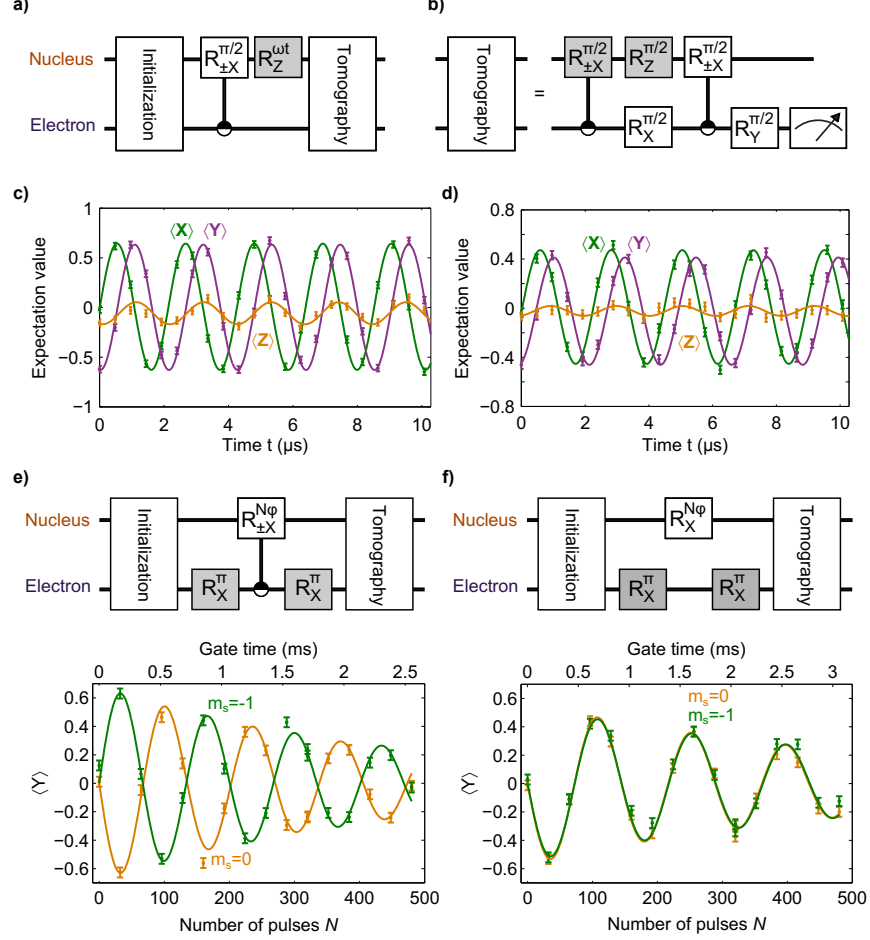


Figure 2: Individual nuclear spin control and readout. (a) Sequence for nuclear-spin free-precession experiments. The Z -rotation is implemented by an off-resonant sequence ($\tau = 2\pi/\omega_L$) with a variable number of pulses N . (b) Nuclear spin state tomography is performed by mapping the $\langle X \rangle$, $\langle Y \rangle$ and $\langle Z \rangle$ expectation values onto the electron spin and reading out the electron (shaded gates are optional basis rotations). (c-d) Measurement of $\langle X \rangle$, $\langle Y \rangle$ and $\langle Z \rangle$ as function of the free-evolution time. The oscillations in $\langle X \rangle$ and $\langle Y \rangle$ confirm the selective control and readout of the targeted nuclear spins. The amplitude yields a combined readout and initialization fidelity of 0.82(1) for spin 1 in (c) and 0.72(1) for spin 2 in (d). Curves are sinusoidal fits. See Supplementary Information for a complete data set with three nuclear spins for each of the three NV centres studied, demonstrating the universality of the control method. (e) Characterization of the conditional gate for nuclear spin 1. The nuclear spin rotates about X with opposite directions for $m_s = 0$ (without shaded gates) and $m_s = -1$ (with shaded gates). Time for a $\pm\pi/2$ -rotation: 170 μs . (f) Unconditional gate for nucleus 1; the rotation is independent of the electron state. Time for a $\pi/2$ -rotation: 254 μs . See Supplementary Information for gates on nuclear spin 2. Results are not corrected for initialization or readout fidelities.

kHz for nuclear spin 1 (Fig. 2c) and $\omega = 2\pi \cdot 449(2)$ kHz for nuclear spin 2 (Fig. 2d), are different and agree with the average of $\omega = \omega_L$ (for $m_s = 0$) and $\omega \approx \omega_L + A_{\parallel}$ (for $m_s = -1$), as expected because the electron spin is continuously flipped. A_{\parallel} is the parallel component of the hyperfine interaction (Methods) and $\omega_L = 2\pi \cdot 431$ kHz is the bare nuclear Larmor frequency. These results confirm that we selectively address the two targeted ^{13}C spins.

Universal control requires both conditional and unconditional gates, while maintaining a high degree of coherence for all qubits in the register. To characterize our gates, we initialize the nuclear spins, prepare the electron spin either in $m_s = 0$ or in $m_s = -1$ and apply a gate with a variable number of pulses. For the conditional gate, $\langle Y \rangle$ oscillates in anti-phase for the two electron states: the nuclear spin rotates around X in a direction that depends on the initial electron state (Fig. 2e). In contrast, for the unconditional gate the rotation direction is independent of the electron state (Fig. 2f). The slow decay of the oscillations indicates that high gate fidelities are possible ($F \sim 0.96$ for a nuclear $\pi/2$ -rotation), enabling us to explore multi-gate sequences that implement nuclear-nuclear gates and quantum

FIGURE 3

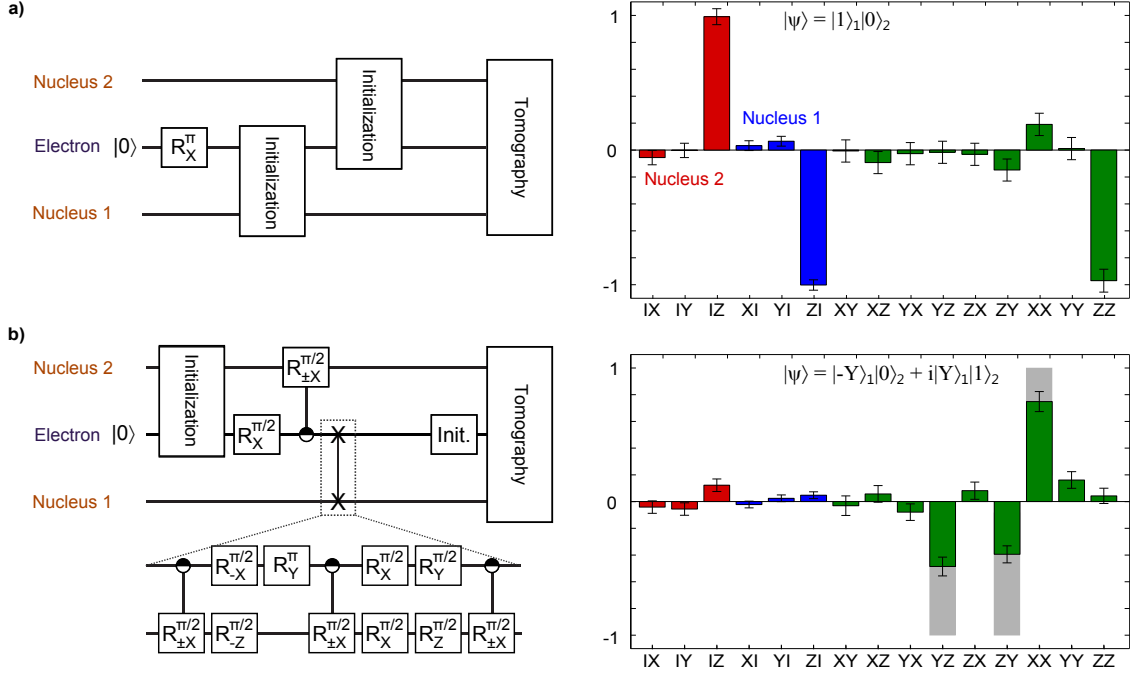


Figure 3: Two-qubit control and nuclear-nuclear entangling gate. (a) The nuclear spins are prepared in $|1\rangle_1|0\rangle_2$ and two-qubit tomography is performed by mapping the 15 combinations of Pauli operators $\langle\sigma_i\sigma_j\rangle$ onto the electron spin (Supplementary Information). After correction for single-qubit initialization and readout fidelities, the state fidelity with the target state is $F = 0.99(3)$, indicating that the sequential initialization and two-qubit readout are accurate. (b) Entangling gate between nuclear spins by coherently swapping the state of the electron onto nuclear spin 1. The gate consists of 167 electron operations over $986\ \mu\text{s}$ (excluding initialization and tomography). The nuclear spin coherence is preserved during electron spin re-initialization (a $2\ \mu\text{s}$ laser pulse); T_2^* values under illumination are $51(7)\ \mu\text{s}$ and $0.35(9)\ \text{ms}$ for nuclear spin 1 and 2 respectively (Supplementary Information). The grey bars depict the target state.

error correction.

To realize quantum gates between the nuclear spins [27,29], whose mutual interaction is negligible, we use the electron spin as a quantum bus. We first verify that both nuclear spins can be prepared and read out in the same experiment by initializing the spins in an eigenstate and performing state tomography by mapping the two-qubit correlations onto the electron spin (Fig. 3a). We then implement entangling gates through an electron controlled gate on nuclear spin 2 and a subsequent coherent SWAP gate between the electron and nuclear spin 1 (Fig. 3b). The tomography reveals strong correlations between the nuclear spins with near-zero single-qubit expectation values, a clear signature of an entangling gate. The fidelity with the target state is $0.66(3)$ (initialization and readout corrected), demonstrating that the gate can take a pure input state into an entangled state of nuclear spins.

Finally, we implement a quantum-error-correction protocol that protects a quantum state from bit-flip errors by encoding it in a 3-qubit state and correcting errors through majority voting (Fig. 4a). Such protocols have been realized with nuclear magnetic resonance [14,15], trapped ions [16] and superconducting qubits [17], but have so far been out of reach for individual solid-state spins due to a lack of multi-qubit control. We compose this protocol from one- and two-qubit gates (Fig. 4b) and separately confirm that the constructed doubly-controlled gate flips the state around X only if the control qubits (nuclear spins) are in $|1\rangle_1|1\rangle_2$ (Fig. 4c).

We first characterize the effect of errors on each individual qubit. The applied errors are rotations around the X-axis by an angle θ with a random sign (50% clockwise, 50% anticlockwise) and therefore represent a decoherence-type process with a strength determined by θ . We prepare 6 input states $|\psi\rangle = |\pm X\rangle, |\pm Y\rangle$ and $|\pm Z\rangle$, measure the corresponding fidelities F of the output states and calculate the process fidelity F_p with the identity process:

$$F_p = \frac{F_x + F_{-x} + F_y + F_{-y} + F_z + F_{-z}}{4} - 1/2$$

Without error correction, errors on the data qubit (electron spin) are expected to result in an oscillation about

FIGURE 4

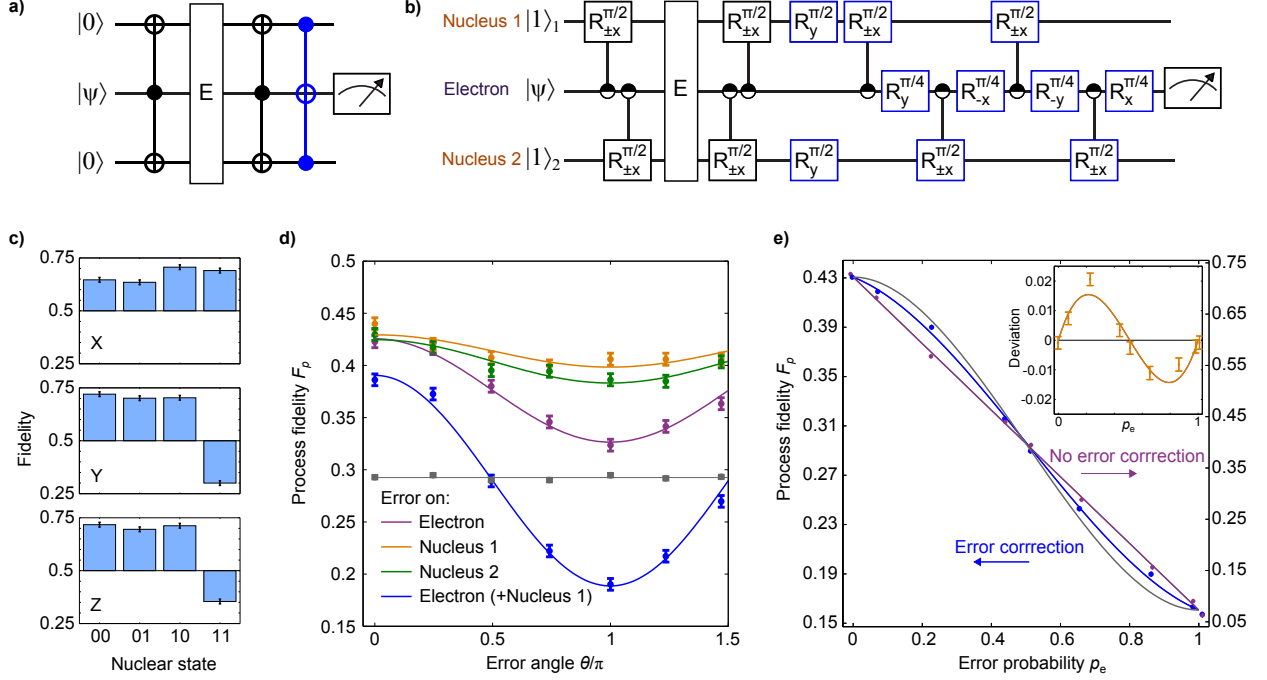


Figure 4: Implementation of 3-qubit quantum error correction. (a) Bit-flip quantum-error-correction protocol. The state $|\psi\rangle$ is encoded in an entangled state using two ancilla qubits. Potential errors E are detected by decoding and are corrected based on a doubly-controlled NOT gate. (b) Our implementation of the quantum-error-correction protocol in (a). The doubly-controlled gate (blue) is constructed using 4 controlled gates as the final ancilla states are irrelevant. The experiment consists of 308 electron operations in 1.8 ms (excluding initialization). (c) Characterization of the doubly-controlled gate (blue gates in (b) only). The average output fidelities for $|\pm X\rangle$, for $|\pm Y\rangle$ and for $|\pm Z\rangle$ are shown for the four ancilla basis states. The average process fidelity with the targeted action is $F_p = 0.534(5)$. (d) Process fidelity for errors applied to nucleus 1, to nucleus 2, or to the electron spin (with and without additional flip of nuclear spin 1). Grey data and fit are $F_{p0} = (F_x + F_{-x})/4$ which sets the average value for the expected oscillations if no errors are corrected. (e) Process fidelity for errors simultaneously applied to all three qubits with error probability p_e . Purple: without error correction. Blue: with error correction. Grey: for ideal robustness against errors. Error bars are given by the symbol size (typical standard deviation 0.002). Inset: deviation of the error correction data from a linear curve. All curves in (d) and (e) are fits to the model in the Methods section.

$F_{p0} = (F_x + F_{-x})/4$ because only the $|\pm X\rangle$ states are unaffected by the applied errors. Instead, the experimental process fidelity with error correction always remains above F_{p0} , even for a completely randomizing error ($\theta = \pi/2$), indicating that the state is partly recovered (Fig. 4d). If one of the ancilla qubits (nuclear spins) is also flipped, an oscillation about F_{p0} is observed; the error correction is effectively turned off because the protocol cannot correct two-qubit errors.

To quantitatively determine the effectiveness of the error correction we analyze it in terms of the three probabilities p_n that an applied error on qubit n is successfully corrected and a decoherence/depolarization process during the error-correction protocol itself (Methods). The model accurately fits the data and gives $p_1 = 0.63(1)$, $p_2 = 0.89(2)$ and $p_3 = 0.84(2)$ for errors on the electron, nucleus 1 and nucleus 2 respectively. Crucially, the average probability $\langle p_n \rangle = (p_1 + p_2 + p_3)/3 = 0.786(9)$ is well above $2/3$, demonstrating that the process is robust against applied single-qubit errors and that the entropy associated with the errors is successfully shuttled to the ancilla qubits.

We further demonstrate the robustness by applying errors simultaneously on all three qubits (Fig. 4e). Without error correction, i.e. without doubly-controlled gate, a linear dependence is observed and a fit to the expected form gives $\langle p_n \rangle = 0.67(3)$ in excellent agreement with $\langle p_n \rangle = 2/3$ expected for no robustness to errors. With error correction a markedly slower initial decay and a non-linear behaviour with $\langle p_n \rangle = 0.84(3)$ is obtained. This suppression of the linear dependence is a key characteristic of quantum error correction.

The deviation from $\langle p_n \rangle = 1$ is mainly due to imperfect nuclear initialization, which might be improved by repeated initialization steps (Supplementary Information) or projective measurements [9,21]. We calculate $\langle p_n \rangle = 0.94(2)$ for ideal initialization fidelity (Supplementary Information). Without applied errors, decoherence and depolarization

during the protocol itself (more than 300 electron operations over 1.8 ms) result in a process fidelity of $F_p = 0.431(2)$, corresponding to an average gate fidelity of 0.93 for the 10 nuclear spin gates. The main source of infidelity is electron decoherence ($T_{coh} = 2.86(4)$ ms, Fig. 1b), which is likely phonon-induced [30] and limits the average gate fidelity to 0.97. Nuclear spin dephasing further reduces the fidelity to 0.94, close to the observed value (Supplementary Information). The electronic coherence time is greatly increased at cryogenic temperatures, at which $T_{coh} = 14$ ms (single NV) [18] and $T_{coh} = 0.6$ s (ensembles) [30] have already been reported. Nuclear spin dephasing can be mitigated by decoupling nuclear-nuclear interactions (T_2 measurements in Supplementary Information). With such future improvements, our results can be used to protect entangled states of solid-state spins.

In conclusion, we have established universal control over weakly coupled nuclear spins that were previously regarded as a source of decoherence. These results provide multiple qubits per defect with high certainty and are compatible with control of the intrinsic nitrogen spin and potential strongly coupled ^{13}C spins. Our techniques can be applied to a wide variety of other electron-nuclear spin systems [2,3,10,13]. The resulting reliable multi-qubit registers can be combined with recently demonstrated coherent coupling between (distant) electron spins [11,18] to realize novel surface-code quantum-computation architectures that use four qubits per defect node [19] and extended quantum networks for long-distance quantum communication.

METHODS

Diamond sample and hyperfine interactions

We use a room-temperature type IIa diamond with 1.1% of ^{13}C grown by chemical vapor deposition (Element 6). We apply a magnetic field of $B_z \approx 403$ G along the NV symmetry axis (Z -axis), yielding a ^{13}C Larmor frequency $\omega_L = 2\pi \cdot 431$ kHz. The electronic dephasing time T_2^* is $3.3(1)$ μs . The hyperfine interaction for nuclear spin i is given by $A_i = A_{\parallel}^i \hat{z} + A_{\perp}^i \hat{x}$ (Fig. 1a), with A_{\parallel} the component parallel to the magnetic field and A_{\perp} the perpendicular component. $A_{\parallel}^1 = 2\pi \cdot 78.2(8)$ kHz and $A_{\perp}^1 = 2\pi \cdot 30(1)$ kHz for nuclear spin 1, and $A_{\parallel}^2 = 2\pi \cdot 32(3)$ kHz and $A_{\perp}^2 = 2\pi \cdot 44(2)$ kHz for nuclear spin 2. Because $A_{\parallel}, A_{\perp} < (2\sqrt{2})/T_2^* = 2\pi \cdot 136(1)$ kHz the nuclear spins are weakly coupled to the electron spin and the hyperfine splittings are unresolved.

Nuclear gate design

In a suitable rotating frame, the Hamiltonian with a single nuclear spin can be written:

$$\hat{H} = |0\rangle\langle 0|\hat{H}_0 + |1\rangle\langle 1|\hat{H}_1$$

with $\hat{H}_0 = \omega_L \hat{I}_Z$ and $\hat{H}_1 = (\omega_L + A_{\parallel})\hat{I}_Z + A_{\perp}\hat{I}_X$ and with $|0\rangle$ and $|1\rangle$ the $m_s = 0$ and $m_s = -1$ electron states, respectively. Nuclear spin gates are performed by applying sequences of the type $(\tau - \pi - 2\tau - \pi - \tau)^{(N/2)}$ on the electron spin (Rabi frequency 31.25 MHz). Because we set $\omega_L \gg A_{\perp}$, sharp resonances occur at $\tau \approx \frac{k\pi}{2\omega_L + A_{\parallel}}$, with integer k . At these values a nuclear X -rotation is performed (assuming $A_{\perp} \neq 0$). For odd k the direction of the rotation is conditional on the electron spin (e.g. the $R_{\pm X}^{\pi/2}$ gates), for even k it is unconditional ($R_X^{\pi/2}$ gates). For the conditional gates we use $\tau = 2.656$ μs , $N = 32$ for spin 1 and $\tau = 3.900$ μs , $N = 18$ for spin 2. For the unconditional gates we use $\tau = 3.186$ μs , $N = 40$ for spin 1 and $\tau = 2.228$ μs , $N = 64$ for spin 2. Z -rotations are implemented by choosing τ off-resonant. Detailed simulations of the nuclear spin dynamics are available in the Supplementary Information.

Nuclear spin initialization fidelity

The electron Ramsey measurements in Fig. 1d and 1e are analyzed in two ways: (1) The measurements are separately fit to $F = 1/2 - 1/2e^{-(t/T_2^*)^2} \cos(\omega t)$, in which T_2^* is a measure for the dephasing time set by the entire spin bath. The external magnetic field stability of better than 2 mG over the total integration time (~ 2 hours), required in these experiments, was achieved by post selecting from a larger measurement set. (2) We determine the nuclear spin initialization fidelities F_1 and F_2 by averaging over multiple measurement runs (Supplementary Information) and using the hyperfine components A_{\parallel}^1 and A_{\parallel}^2 together with:

$$F = 1/2 - 1/2e^{-(t/T_2^{**})^2} \left(F_1 F_2 \cos \left[\left(\omega + \frac{A_{\parallel}^1 + A_{\parallel}^2}{2} \right) t \right] + F_1 (1 - F_2) \cos \left[\left(\omega + \frac{A_{\parallel}^1 - A_{\parallel}^2}{2} \right) t \right] \right. \\ \left. + (1 - F_1) F_2 \cos \left[\left(\omega + \frac{-A_{\parallel}^1 + A_{\parallel}^2}{2} \right) t \right] + (1 - F_1)(1 - F_2) \cos \left[\left(\omega - \frac{A_{\parallel}^1 + A_{\parallel}^2}{2} \right) t \right] \right).$$

Here $T_2^{**} = 4.5(3) \mu\text{s}$ is the electronic dephasing due to the rest of the spin bath, i.e. not including the two spins under study.

Quantum error correction analysis

The applied errors realize the quantum map:

$$E(\rho, \theta) = \cos^2(\theta/2) I \rho I + \sin^2(\theta/2) X \rho X,$$

in which ρ is the initial density matrix (error characterization in Supplementary Information). We analyze the error-correction protocol by separating depolarization during the encoding, decoding and error-correction steps from the robustness of the encoded state to applied errors, which is characterized by the three probabilities p_n that an error applied on qubit n is successfully corrected (derivation in Supplementary Information). The process fidelity for a single-qubit error (Fig. 4d) is then given by:

$$F_p(\theta) = F_{p0} + A_{YZ}[p_n + (1 - p_n) \cos \theta],$$

where $F_{p0} = (F_x + F_{-x})/4$ and $A_{YZ} = (F_y + F_{-y} + F_z + F_{-z} - 2)/4$ characterize the additional depolarization and are given by the average fidelities without applied errors. The equation contains a constant due to the $|\pm X\rangle$ states, which are unaffected by the applied error, and a sum of successful ($p_n = 1$) and unsuccessful ($p_n = 0$) error correction for the $|\pm Y\rangle$ and $|\pm Z\rangle$ states. For errors simultaneous on all three qubits (Fig. 4e), the process fidelity becomes:

$$F_p(p_e) = F_{p0} + A_{YZ}[1 - 3p_e + 3p_e^2 - 2p_e^3 + 3(2\langle p_n \rangle - 1)(p_e - 3p_e^2 + 2p_e^3)],$$

with $p_e = \sin^2(\theta/2)$ the error probability. In general this equation describes a third order polynomial. For ideal error correction ($\langle p_n \rangle = 1$) the linear term vanishes, whereas without robustness to errors ($\langle p_n \rangle = 2/3$), the result is strictly linear. The inversion symmetry about $p_e = 0.5$ observed both theoretically and experimentally ensures that the nonlinear behavior is not due to spurious coherent rotations.

NOTE

After submission of this manuscript we became aware of related work by Waldherr et al., arXiv:1309.6424 in which 3-qubit quantum error correction is implemented using strongly coupled nuclear spins.

ACKNOWLEDGEMENTS

We thank L. Childress, J. J. L. Morton, O. Moussa and L.M.K. Vandersypen for helpful discussions and comments. T.H.T. acknowledges support by a Marie Curie Intra European Fellowship within the 7th European Community Framework Programme. Work at the Ames Laboratory was supported by the U.S. Department of Energy Basic Energy Sciences under contract no. DE-AC02-07CH11358. We acknowledge support from the Dutch Organization for Fundamental Research on Matter (FOM), the Netherlands Organization for Scientific Research (NWO), the DARPA QuASAR programme, the EU SOLID, and DIAMANT programmes and the European Research Council through a Starting Grant.

REFERENCES

- [1] Awschalom, D.D., Bassett, L.C., Dzurak, A.S., Hu, E.L., & Petta, J.R., Quantum Spintronics: Engineering and Manipulating Atom-Like Spins in Semiconductors. *Science* **339**, 1174-1179 (2013).
- [2] Koehl, W.F., Buckley, B.B., Heremans, F.J., Calusine, G., & Awschalom, D.D., Room temperature coherent control of defect spin qubits in silicon carbide. *Nature* **479**, 84-87 (2011).
- [3] Yin, C. et al., Optical addressing of an individual erbium ion in silicon. *Nature* **497**, 91-94 (2013).
- [4] Gurudev Dutt, M.V. et al., Quantum Register Based on Individual Electronic and Nuclear Spin Qubits in Diamond. *Science* **316**, 1312-1316 (2007).
- [5] Neumann, P. et al., Multipartite Entanglement Among Single Spins in Diamond. *Science* **320**, 1326-1329 (2008).
- [6] Fuchs, G.D., Burkard, G., Klimov, P.V., & Awschalom, D.D., A quantum memory intrinsic to single nitrogen-vacancy centres in diamond. *Nature Phys.* **7**, 789-793 (2011).
- [7] van der Sar, T. et al., Decoherence-protected quantum gates for a hybrid solid-state spin register. *Nature* **484**, 82-86 (2012).
- [8] Maurer, P.C. et al., Room-Temperature Quantum Bit Memory Exceeding One Second. *Science* **336**, 1283-1286 (2012).
- [9] Pfaff, W. et al., Demonstration of entanglement-by-measurement of solid-state qubits. *Nature Phys.* **9**, 29-33 (2013).
- [10] Pla, J.J. et al., High-fidelity readout and control of a nuclear spin qubit in silicon. *Nature* **496**, 334-338 (2013).
- [11] Dolde, F. et al., Room-temperature entanglement between single defect spins in diamond. *Nature Phys.* **9**, 139-143 (2013).
- [12] Jiang, L. et al., Repetitive Readout of a Single Electronic Spin via Quantum Logic with Nuclear Spin Ancillae. *Science* **326**, 267-272 (2009).
- [13] Lee, S.-Y. et al., Readout and control of a single nuclear spin with a metastable electron spin ancilla. *Nature Nanotech.* **8**, 487-492 (2013).
- [14] Cory, D.G. et al., Experimental Quantum Error Correction. *Phys. Rev. Lett.* **81**, 2152-2155 (1998).
- [15] Moussa, O., Baugh, J., Ryan, C.A., & Laflamme, R., Demonstration of Sufficient Control for Two Rounds of Quantum Error Correction in a Solid State Ensemble Quantum Information Processor. *Phys. Rev. Lett.* **107**, 160501 (2011).
- [16] Schindler, P. et al., Experimental Repetitive Quantum Error Correction. *Science* **332**, 1059-1061 (2011).
- [17] Reed, M.D. et al., Realization of three-qubit quantum error correction with superconducting circuits. *Nature* **482**, 382-385 (2012).
- [18] Bernien, H. et al., Heralded entanglement between solid-state qubits separated by three metres. *Nature* **497**, 86-90 (2013).
- [19] Nickerson, N.H., Li, Y., & Benjamin, S.C., Topological quantum computing with a very noisy network and local error rates approaching one percent. *Nat. Commun.* **4**, 1756 (2013).
- [20] Neumann, P. et al., Single-Shot Readout of a Single Nuclear Spin. *Science* **329**, 542-544 (2010).
- [21] Robledo, L. et al., High-fidelity projective read-out of a solid-state spin quantum register. *Nature* **477**, 574-578 (2011).
- [22] Dreau, A., Spinicelli, P., Maze, J.R., Roch, J.F., & Jacques, V., Single-Shot Readout of Multiple Nuclear Spin Qubits in Diamond under Ambient Conditions. *Phys. Rev. Lett.* **110**, 060502 (2013).
- [23] Taminiau, T.H. et al., Detection and Control of Individual Nuclear Spins Using a Weakly Coupled Electron Spin. *Phys. Rev. Lett.* **109**, 137602 (2012).
- [24] Kolkowitz, S., Unterreithmeier, Q.P., Bennett, S.D., & Lukin, M.D., Sensing Distant Nuclear Spins with a Single Electron Spin. *Phys. Rev. Lett.* **109**, 137601 (2012).
- [25] Zhao, N. et al., Sensing single remote nuclear spins. *Nature Nanotech.* **7**, 657-662 (2012).
- [26] Hodges, J.S., Yang, J.C., Ramanathan, C., & Cory, D.G., Universal control of nuclear spins via anisotropic hyperfine interactions. *Phys. Rev. A* **78**, 010303 (2008).
- [27] Zhang, Y., Ryan, C.A., Laflamme, R., & Baugh, J., Coherent Control of Two Nuclear Spins Using the Anisotropic Hyperfine Interaction. *Phys. Rev. Lett.* **107**, 170503 (2011).
- [28] London, P. et al., Detecting and polarizing nuclear spins with double resonance on a single electron spin. *Phys. Rev. Lett.* **111**, 067601 (2013).
- [29] Filidou, V. et al., Ultrafast entangling gates between nuclear spins using photoexcited triplet states. *Nature Phys.* **8**, 596-600 (2012).

[30] Bar-Gill, N., Pham, L.M., Jarmola, A., Budker, D., & Walsworth, R.L., Solid-state electronic spin coherence time approaching one second. *Nat. Commun.* **4**, 1743 (2013).

SUPPLEMENTARY MATERIAL

SETUP AND SAMPLE

The experimental setup and sample are described in detail in the supplementary information of Van der Sar et al. [1] We used a type-IIa chemical vapour deposition grown diamond with a 1.1% natural abundance of carbon-13 (Element 6). Solid immersion lenses were fabricated on top of the nitrogen vacancy (NV) centres to enhance the collection efficiency [2]. The electron spin is controlled by microwaves through an on-chip stripline (Rabi frequency of 31.25 MHz). A magnetic field of $B_z \approx 403$ G was applied along the NV symmetry axis using three electromagnets. At this magnetic field the intrinsic NV nitrogen-14 spin is polarized due to an excited-state anti-crossing [3, 4].

ELECTRON SPIN INITIALIZATION AND READOUT

This section discusses the electron spin initialization, re-initialization and readout. In particular it analyzes how the imperfect spin and charge state initialization affect the outcomes of the different type of experiments performed.

Experimental

The electron spin is initialized in the $m_s = 0$ state by a 532 nm ($\sim 150\mu\text{W}$) laser pulse (typically $4\mu\text{s}$) and read out through its spin-dependent time-resolved fluorescence. In all experiments we measure the difference signal $\Delta_f = S_f - \tilde{S}_f$ between the fluorescence signal S_f for the final state and the fluorescence signal \tilde{S}_f for the final state with a pi-pulse applied just before readout ($m_s = 0$ to $m_s = -1$ transition). The obtained value is then normalized by dividing it by the same difference signal right after initialization: $\Delta_i = S_i - \tilde{S}_i$, where S_i is without pi-pulse and \tilde{S}_i with pi-pulse. The final normalized contrast C is:

$$C = \frac{S_f - \tilde{S}_f}{S_i - \tilde{S}_i} = \frac{\Delta_f}{\Delta_i}. \quad (1)$$

This method directly measures the contrast between $m_s = 0$ and $m_s = -1$ states. Note that $-1 \leq C \leq 1$ and that the result is independent of the population in other states, such as $m_s = +1$, that are not affected by the microwave pi-pulse. The reported expectation values directly correspond to C , the measured fidelities are obtained from $F = C/2 + 1/2$.

Initial electron state

The electronic initialization involves both spin states ($m_s = -1, 0, +1$) and charge states (NV^- and NV^0). The initial state ρ_i is:

$$\rho_i = p_1\rho_0 + p_2\rho_m + p_3\rho_s + p_4\rho_c, \quad (2)$$

with $p_1 + p_2 + p_3 + p_4 = 1$, and in which ρ_0 is the desired $m_s = 0$ state, ρ_m is the completely mixed state of $m_s = 0$ and $m_s = -1$, ρ_s represents the other spins states (here $m_s = +1$) and ρ_c other charge states (here NV^0).

The precise values for p_1, p_2, p_3 and p_4 are unknown. For this NV centre the spin-state initialization fidelity was previously reported to be $F_s = \frac{p_1 + p_2/2}{p_1 + p_2 + p_3} > 0.95$ under similar conditions [1]. The NV^- charge-state initialization fidelity $F_c = p_1 + p_2 + p_3$ is unknown here, but values of ~ 0.7 have been reported for other NV centres [8].

The available initial population is given by p_1 . Ideally, measurements of $C = \frac{\Delta_f}{\Delta_i}$ directly reflect the actual polarization so that $-p_1 \leq C \leq p_1$. Because only the ρ_0 term in equation 2 is affected by microwave pulses only this term yields signal (non-zero Δ), so that the normalization signal always is $\Delta_i = D_0 p_1$, with D_0 an unknown proportionality constant. Next we determine the obtainable final signal Δ_f for two types of experiments: experiments that do not re-initialize the electron to create additional polarization in the nuclear spin register and those that do.

Experiments without nuclear spin initialization

First consider experiments where only a single electron initialization step is used, i.e. experiments that do not transfer polarization to the nuclear spins before resetting the electron spin. In this case the maximum value of Δ_f simply is $D_0 p_1$ and the maximum contrast is $C_{max} = \frac{D_0 p_1}{D_0 p_1} = 1$. Due to the calibration, the final measured contrast is independent of p_1 and therefore does not take into account the charge and spin initialization fidelities.

Experiments with nuclear spin initialization

Now consider experiments in which the electron spin polarization is transferred to a nuclear spin, the electron is re-initialized, and finally the electron is used to measure the nuclear spin state. The result Δ_f depends on the correlations of the spin (charge) state after the re-initialization step with the spin (charge) state before it. We assume the spin states before and after re-initialization are uncorrelated, and derive the result Δ_f for both uncorrelated (no memory) and maximally positive correlations (ideal memory) for the charge state.

The state of the initialized electron and a single nuclear spin in a completely mixed state is:

$$\rho = \rho_{electron} \otimes \rho_{nucleus} = p_1(\rho_0 \otimes \rho_m) + p_2(\rho_m \otimes \rho_m) + p_3(\rho_s \otimes \rho_m) + p_4(\rho_c \otimes \rho_m), \quad (3)$$

swapping the electron and nuclear spin states gives:

$$\rho = p_1(\rho_m \otimes \rho_0) + p_2(\rho_m \otimes \rho_m) + p_3(\rho_s \otimes \rho_m) + p_4(\rho_c \otimes \rho_m), \quad (4)$$

as the SWAP gate has no effect on the erroneous electron spin (ρ_s) and charge (ρ_c) states. The electron spin initialization p_1 is thus directly transferred to the nuclear spin.

We re-initialize the electron spin and assume that electron spin initialization is independent of the nuclear spin state. First consider the case of no correlations (no memory) for the charge state, so that the electron is completely re-initialized. The state in equation 4 becomes:

$$\rho = (p_1 \rho_0 + p_2 \rho_m + p_3 \rho_s + p_4 \rho_c) \otimes (p_1 \rho_0 + (1 - p_1) \rho_m). \quad (5)$$

Reading out the nuclear spin with the electron spin only yields non-zero signal for both the electron and nuclear spins in the pure state ρ_0 , so that:

$$\Delta_f = D_0 p_1^2, \quad C_{max} = p_1, \quad (6)$$

which shows that the maximum contrast C_{max} is reduced by a factor p_1 and thus that the experiment faithfully reflects the actual nuclear spin state, including a reduced fidelity due to the imperfect electron spin and charge initialization.

If the electron re-initialization does not change the charge state, equation 4 after electron re-initialization becomes:

$$\rho = p_1 \left(\frac{p_1 \rho_0 + p_2 \rho_m + p_3 \rho_s}{p_1 + p_2 + p_3} \right) \otimes \rho_0 + (p_2 + p_3) \left(\frac{p_1 \rho_0 + p_2 \rho_m + p_3 \rho_s}{p_1 + p_2 + p_3} \right) \otimes \rho_m + p_4 \rho_c \otimes \rho_m \quad (7)$$

Again taking into account that no difference signal is obtained if either the electron or the nuclear spin is not in state ρ_0 :

$$\Delta_f = \frac{p_1^2}{p_1 + p_2 + p_3}, \quad C_{max} = \frac{p_1}{p_1 + p_2 + p_3} \quad (8)$$

The result now accurately reflects the spin state initialization, but is independent of the charge state initialization.

The high nuclear initialization fidelity obtained here ($F \approx 0.9$, figure 1 of the main text), indicates that the charge state initialization fidelity is high (> 0.90) or that the measurements are not sensitive to it (i.e. the re-initialization laser pulse has low probability to change the charge state). The same value gives a lower limit of the electron spin initialization $F = p_1/2 + 1/2 \geq 0.90$, as the swap gate for initialization and the nuclear spin readout have limited fidelities as well.

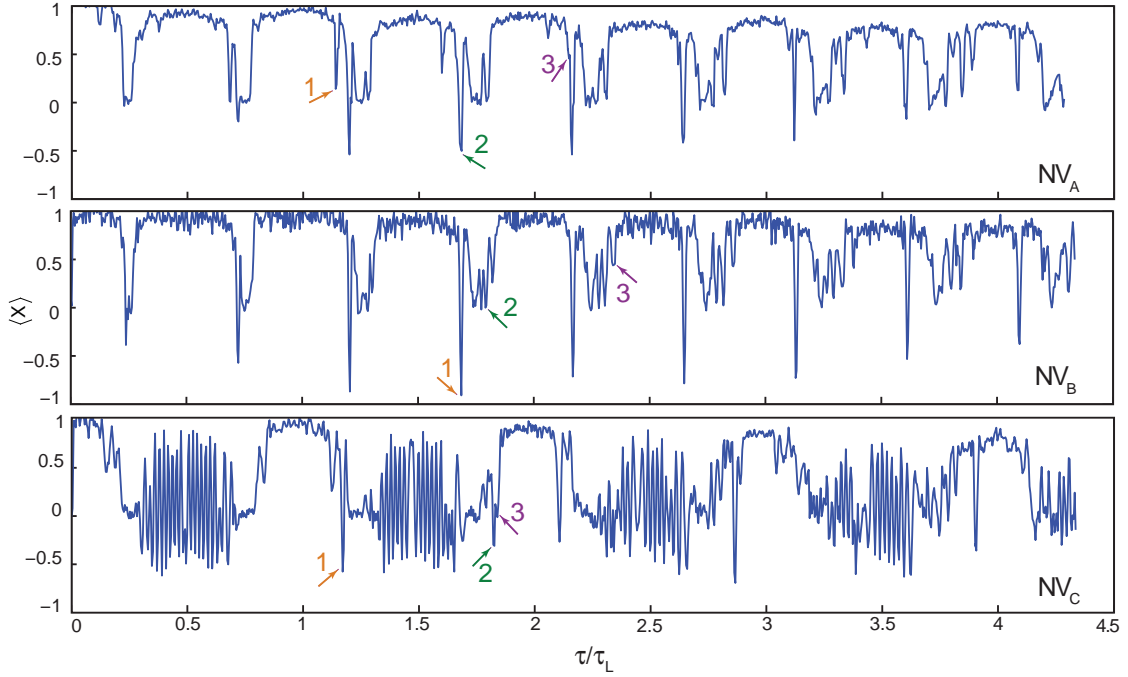


Figure 5: Characterization of the nuclear spin environment for the three NV centres studied. Dynamical decoupling spectroscopy [5] for NV_A , NV_B and NV_C . The electron spin is prepared in a coherent superposition state ($|X\rangle = |0\rangle + |1\rangle$) and a dynamical decoupling sequence with 32 pi-pulses of the form $(\tau - \pi - 2\tau - \pi - \tau)^{16}$ is applied with variable interpulse delay 2τ before measuring $\langle X \rangle$. Sharp dips in the signal indicate an entangling operation of the electron spin with individual ^{13}C spins in the spin bath [5]. The arrows indicate the 9 different ^{13}C nuclear spins, and the values of τ used, for which we implemented initialization, control and readout (see figures 6 for NV_A , 7 for NV_B and 8 for NV_C). The experiments in the main text use nuclear spin 1 and 2 of NV_A . τ_L is the bare Larmor period.

Conclusion

As in previous room temperature experiments, the charge state is thus not rigorously initialized nor proven to be fully reflected in the measurement outcomes. Therefore the measured state fidelities do not give the actual purity of the states and no entanglement can be proven to be present. Nevertheless the (entangling) gates and protocols developed and studied in this work can be accurately investigated through their action on the prepared states. Note that methods to initialize the charge state have been developed at room temperature [8] and that pure entangled states have been reported at cryogenic temperatures using simultaneous spin and charge initialization [10].

CHARACTERIZATION AND CONTROL FOR THREE NV CENTRES

To demonstrate that harnessing weakly coupled spins makes multiple qubits available for each defect with high certainty, we have controlled three weakly coupled nuclear spins for each of the three NV centres studied. This section contains the characterization of the NV centres and the nuclear-spin free-evolution experiments that demonstrate the initialization, control and readout of the nuclear spins.

Characterization of the nuclear spin environment

We use dynamical decoupling spectroscopy [5] to characterize the nuclear spin environment of a total of three NV centres: NV_A , which is studied in the main text, and the two additional centres NV_B and NV_C (Fig. 5). The resulting curves provide characteristic fingerprints of the nuclear spin environments of the NV centre.

NV_A and NV_B show qualitatively similar behavior (Fig. 5); both curves display broad echo collapses due to the spin bath at $\tau/(4\tau_L) = m$ with odd m and show distinct sharp dips due to individual ^{13}C nuclear spins that become

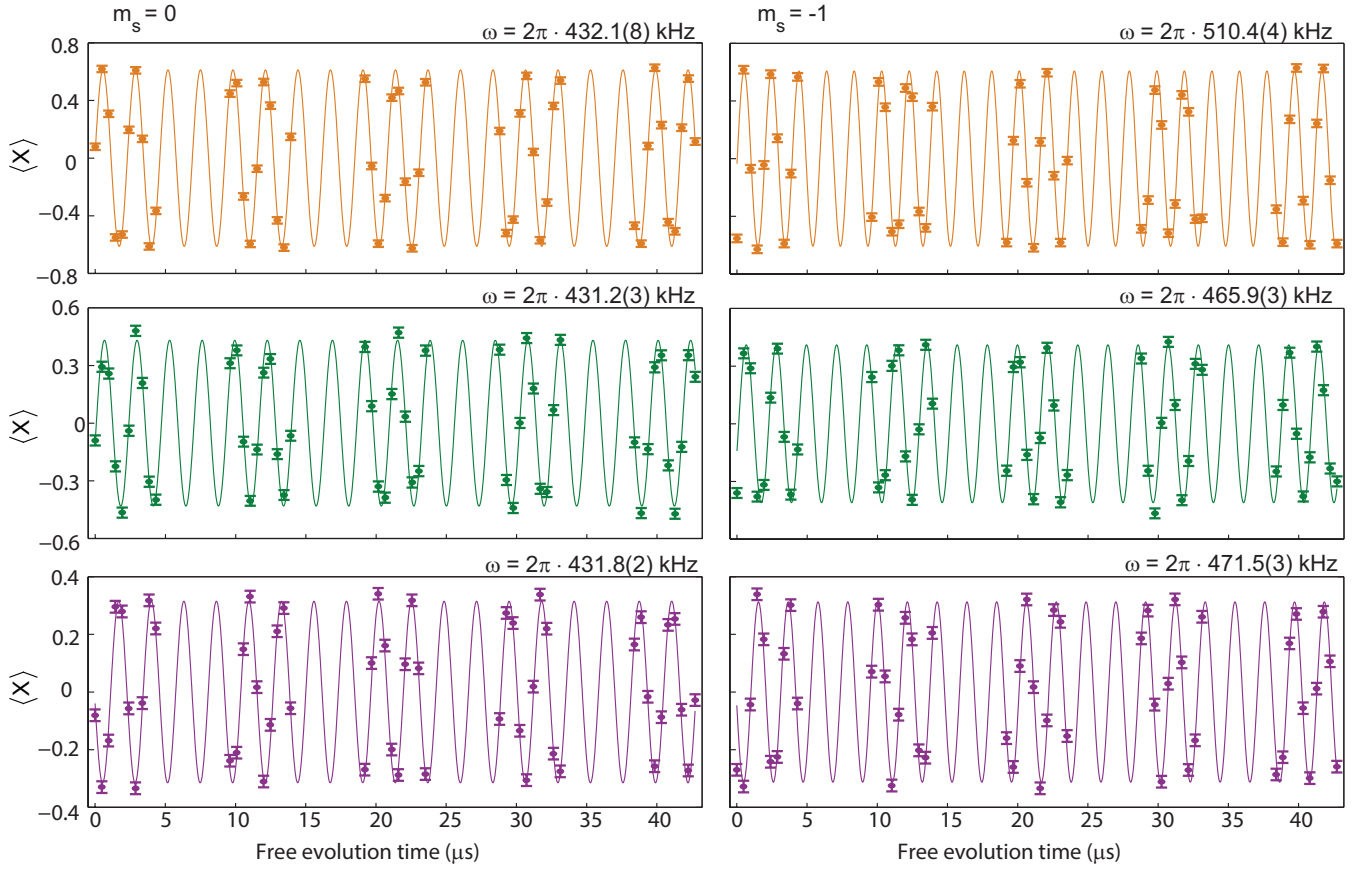


Figure 6: Control of three weakly coupled nuclear spins for NV_A. Experiments as in figure 2 of the main text, but with the electron spin in $m_s = 0$ (left) or $m_s = -1$ (right). The values for τ used for spin 1 (orange), spin 2 (green) and spin 3 (purple) are marked in Fig. 5. Note that nuclear spin 1 and nuclear spin 2 are the two spins studied in detail and used for implementing the quantum-error-correction protocol.

visible at larger τ [5]. However, the positions and depths of the different dips differ strongly due to the characteristic distribution of nuclear spins near each NV centre. In addition to a bath of weakly-coupled ^{13}C spins NV_C shows a rapidly oscillating component in the signal due to the presence of a strongly coupled nuclear spin (hyperfine interaction of $2\pi \cdot 453 \text{ kHz}$).

Control of 3 weakly coupled nuclear spins per NV centre

For each of the three NV centres in figure 5, we select three nuclear spins (marked in the figure) and demonstrate initialization, control and direct readout by performing nuclear free precession experiments (see figures 2a-d of the main text). We prepare the electron spin in $m_s = 0$ or $m_s = -1$. The unique precession frequencies for $m_s = -1$ confirm that in each case three different ^{13}C spins are controlled (Fig. 6, 7 and 8).

These results demonstrate the control of three weakly-coupled nuclear spins for each NV centre studied. Our decoherence-protected gates therefore make several nuclear spins available per defect centre with a high certainty, in stark contrast to the highly probabilistic nature of the presence of strongly coupled ^{13}C spins. The fact that the gates can be applied in the presence of strongly coupled nuclear spins, including the intrinsic Nitrogen and nearby ^{13}C nuclear spins, indicates that quantum registers with over 5 nuclear spins are now well within reach (see e.g. NV_C in figure 5).

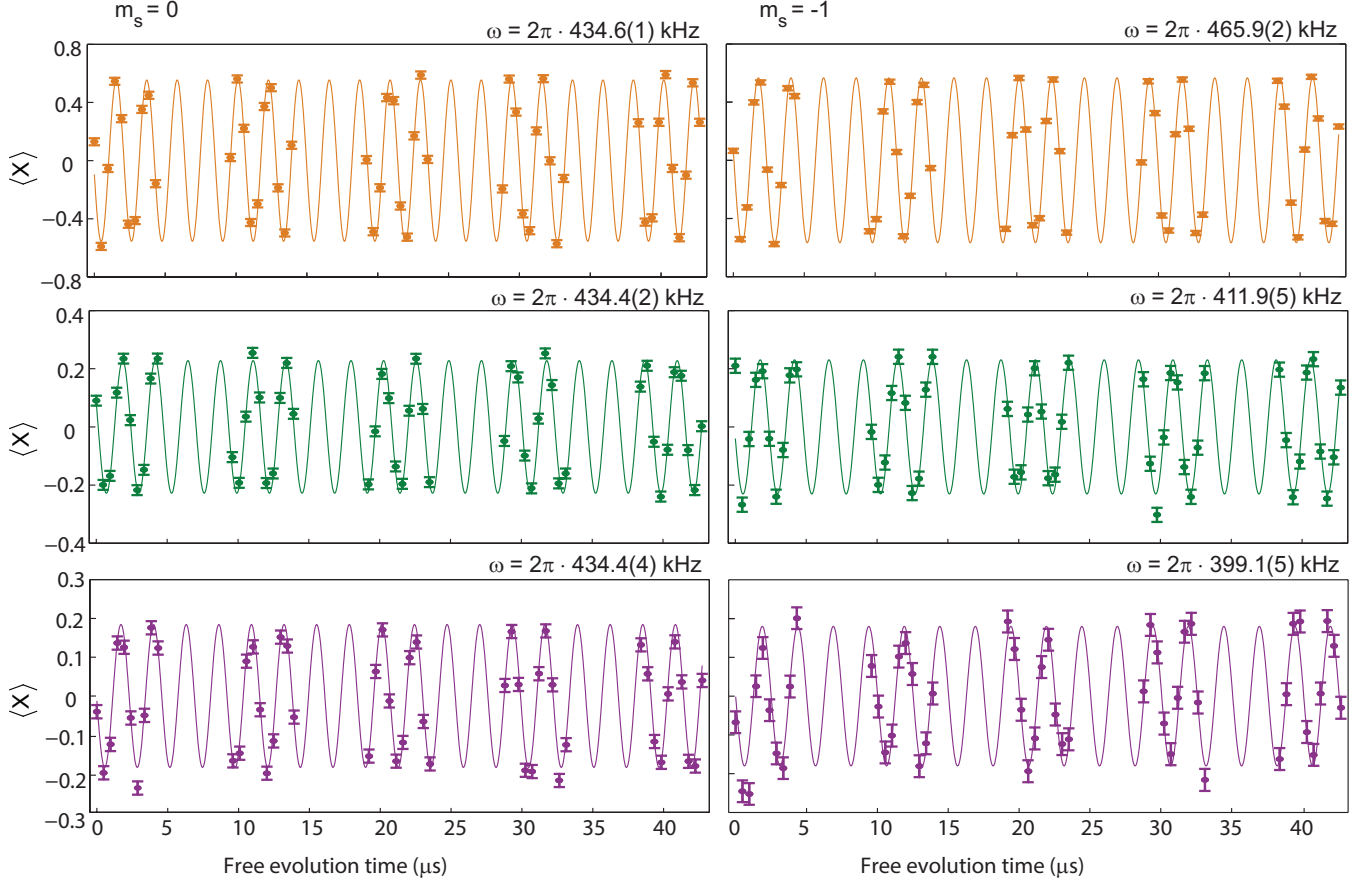


Figure 7: Control of three weakly coupled nuclear spins for NV_B . Experiments as in figure 2 of the main text, but with the electron spin in $m_s = 0$ (left) or $m_s = -1$ (right). The values for τ used for spin 1 (orange), spin 2 (green) and spin 3 (purple) are marked in Fig. 5.

NUCLEAR SPIN DYNAMICS AND GATES

The hyperfine parameters for the three nuclear spins for NV_A , the NV centre used in the main text, are given in Table I. The two nuclear spin qubits in the main text are spin 1 and 2.

Nuclear spin	Parallel component A_{\parallel} (kHz)	Perpendicular component A_{\perp} (kHz)
1	78.2(8)	30(1)
2	32(3)	44(2)
3	41.2(4)	19.2(7)

Table I: Hyperfine parameters for 3 relevant ^{13}C spins. A_{\parallel} is the component parallel to the applied magnetic field (along the NV symmetry axis). A_{\perp} is the perpendicular component. This NV centre was studied previously [5].

Nuclear gate design

With an appropriate rotation of the coordinate axes, the Hamiltonian of the NV electron spin and a single ^{13}C spin is:

$$\hat{H} = A_{\parallel} \hat{S}_z \hat{I}_z + A_{\perp} \hat{S}_z \hat{I}_x + \omega_L \hat{I}_z = |0\rangle\langle 0| \hat{H}_0 + |1\rangle\langle 1| \hat{H}_1, \quad (9)$$

where \hat{S}_i (\hat{I}_i) are the electron (nuclear) spin operators, $\omega_L = 2\pi \cdot 431$ kHz is the nuclear Larmor frequency (applied magnetic field $B_z \approx 403\text{G}$). The nuclear spin evolution thus depends on the electron spin state: \hat{H}_0 if the electron is

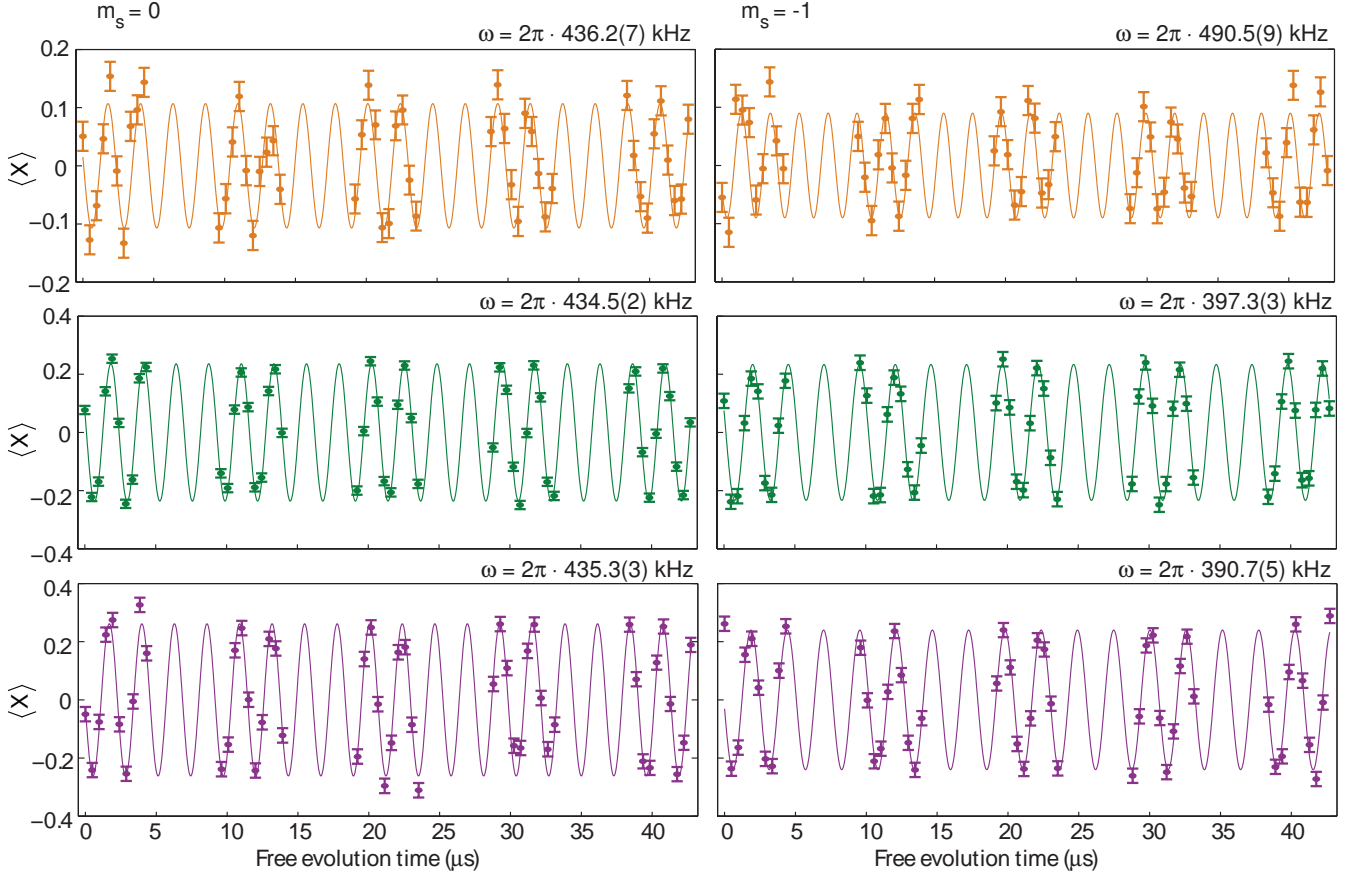


Figure 8: Control of three weakly coupled nuclear spins for NV_C . Experiments as in figure 2 of the main text, but with the electron spin in $m_s = 0$ (left) or $m_s = -1$ (right). The values for τ used for spin 1 (orange), spin 2 (green) and spin 3 (purple) are marked in Fig. 5.

in $m_s = 0$ (state $|0\rangle$), and \hat{H}_1 if the electron is in $m_s = -1$ (state $|1\rangle$), with

$$\hat{H}_0 = \omega_L \hat{I}_z, \quad \text{and} \quad \hat{H}_1 = (A_{\parallel} + \omega_L) \hat{I}_z + B_{\perp} \hat{I}_x. \quad (10)$$

All nuclear gates are implemented by applying the a sequence of periodic pulses on the electron spin:

$$(\tau - \pi - 2\tau - \pi - \tau)^{N/2}, \quad (11)$$

with τ a free evolution time, π a pi-pulse on the electron and N the total number of pulses. We symmetrize the decoupling sequence by alternating pi-pulses around the X and Y axis (base sequence $X - Y - X - Y - Y - X - Y - X$, which is then repeated). The nuclear evolution operators for the basic sequence ($N = 2$) are:

$$\hat{V}_0 = \exp[-i\hat{H}_0\tau] \exp[-i\hat{H}_1 2\tau] \exp[-i\hat{H}_0\tau] \quad (12)$$

$$\hat{V}_1 = \exp[-i\hat{H}_1\tau] \exp[-i\hat{H}_0 2\tau] \exp[-i\hat{H}_1\tau], \quad (13)$$

for $m_s = 0$ and $m_s = -1$ respectively.

The conditional operators \hat{V}_0 and \hat{V}_1 can be represented as:

$$\hat{V}_0 = \exp[-i\phi(\hat{\mathbf{I}} \cdot \hat{\mathbf{n}}_0)] \quad (14)$$

$$\hat{V}_1 = \exp[-i\phi(\hat{\mathbf{I}} \cdot \hat{\mathbf{n}}_1)], \quad (15)$$

which illustrates that the net evolution is a rotation by an angle ϕ around an axis $\hat{\mathbf{n}}_i$ that depends on the initial state of the electron spin: $\hat{\mathbf{n}}_0$ for $m_s = 0$ and $\hat{\mathbf{n}}_1$ for $m_s = -1$. The rotation angle ϕ is independent of the electron spin input state [5]. Next, we show that both conditional and unconditional rotations can be constructed by choosing τ .

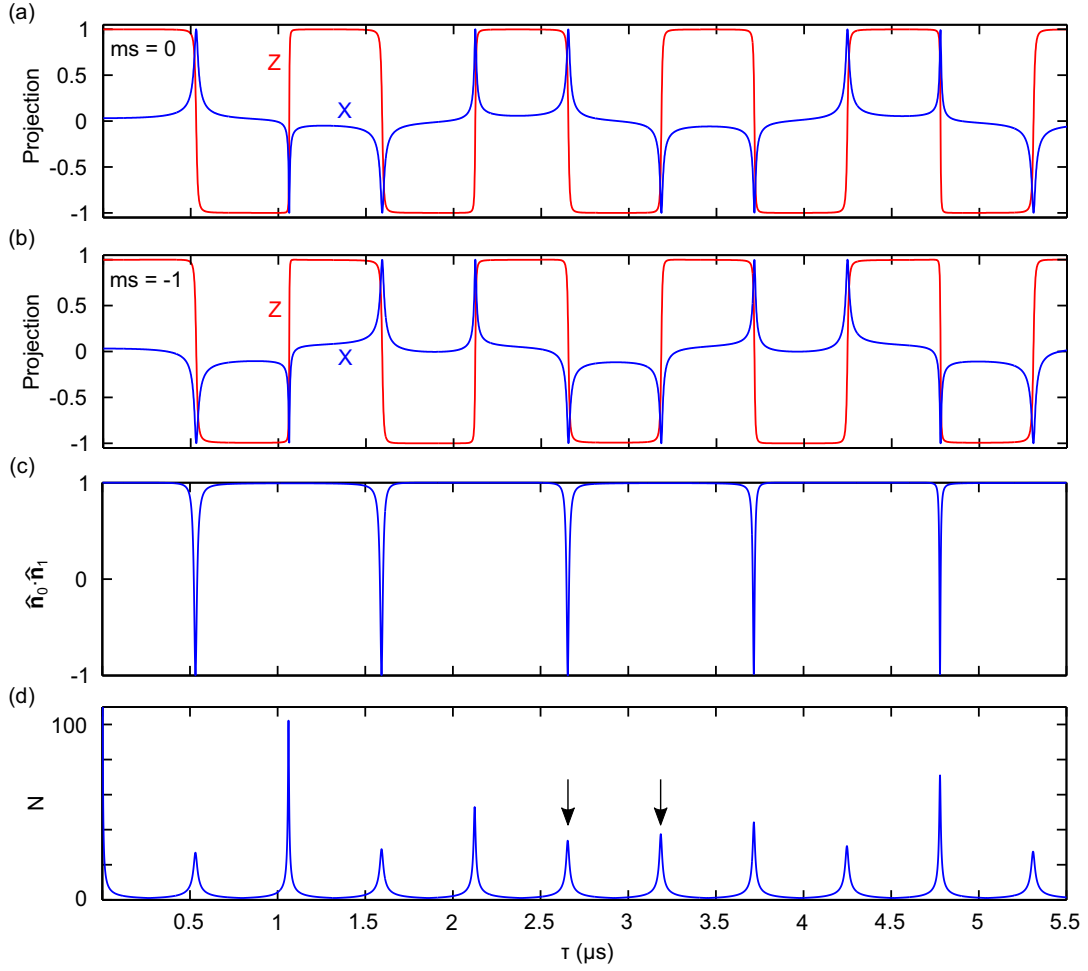


Figure 9: Simulations of the nuclear dynamics for spin 1. (a-b) The X and Z projections of (a) \hat{n}_0 (the net rotation axis for initial electron state $m_s = 0$) and of (b) \hat{n}_1 (initial electron state $m_s = -1$). The Y projection is 0. (c) The inner product $\hat{n}_0 \cdot \hat{n}_1$ of the two rotation axis indicates if the gate is unconditional (parallel axes, $\hat{n}_0 \cdot \hat{n}_1 = 1$) or conditional (anti-parallel axes, $\hat{n}_0 \cdot \hat{n}_1 = -1$). (d) The number of pulses N required for a $\pi/2$ -rotation. The total gate duration is given by $2N\tau$. The two arrows mark the values for τ for the conditional and unconditional gates for this spin.

Figure 9 shows the dynamics for nuclear spin 1. Because $\omega_L \gg A_\perp$, the X and Z components of the rotation axes \hat{n}_0 (Fig. 9a) and \hat{n}_1 (Fig. 9b) show sharp resonances, for which the nuclear spin undergoes an X -rotation. These resonances occur for:

$$\tau \approx \frac{k\pi}{2\omega_L + A_\parallel}, \quad (16)$$

with integer k . The X -rotation is conditional for the odd resonances (odd k , antiparallel rotation axes: $\hat{n}_0 \cdot \hat{n}_1 = -1$) and unconditional for the even resonances (even k , parallel axes: $\hat{n}_0 \cdot \hat{n}_1 = 1$) (Fig. 9c). For all other values of τ the nuclear spin undergoes a simple Z -rotation independent of the electron spin state ($\hat{n}_0 \cdot \hat{n}_1 = 1$). The electron and nuclear spin are then effectively decoupled from each other. The number of pulses N required for a $\pi/2$ rotation are shown in figure 9 as a function of τ . The dynamics for spin 2 are similar (Fig. 10), but the resonances occur for different values of τ due to the difference in A_\parallel .

The values for τ and N for the gates used in this work are given in Table II and the values for τ are also indicated in Figures 9d and 10d.

The sharp resonances enable the universal control of a selected nuclear spin, while decoupling the electron spin from all other nuclear spin qubits and the rest of the environment. The gates are thus selective, not limited by the electron T_2^* or T_2 and do not require strong coupling.

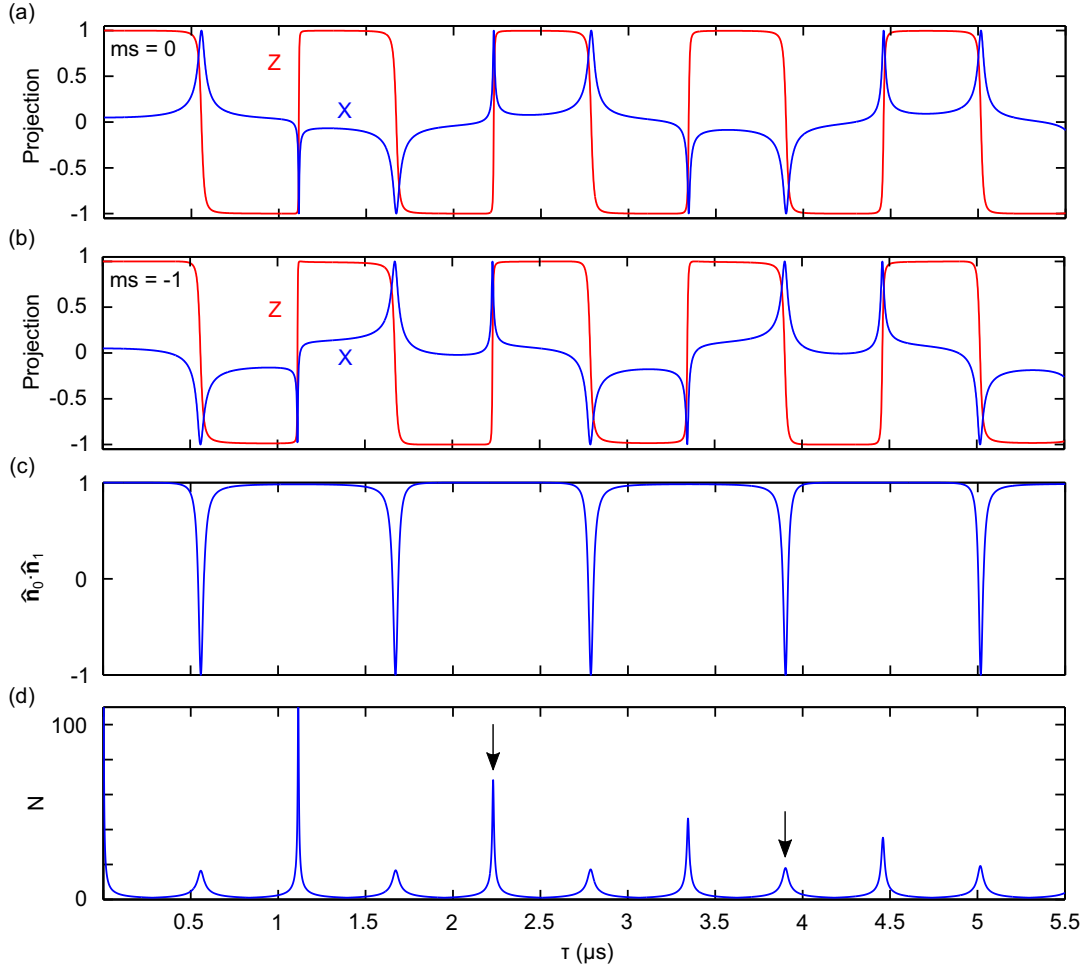


Figure 10: Simulations of the dynamics for nuclear spin 2. See description in figure 9.

	τ (μs)	N	Total time (μs , rounded)
Spin1: $R_X^e(\pi/2)$	2.656	32	170
$R_X(\pi/2)$	3.186	40	255
$R_Z(\pi/2)$	2.058	4	16
Spin2: $R_X^e(\pi/2)$	3.900	18	140
$R_X(\pi/2)$	2.228	64	285
$R_Z(\pi/2)$	2.100	2	8

Table II: Gate parameters. $R_\alpha(\theta)$ is a rotation of the nuclear spin around Bloch-sphere axis α by an angle θ . For gates marked R^e the rotation direction is controlled by the electron spin state, for all other gates the direction is unconditional.

Nuclear gate characterization

To characterize the conditional and unconditional gates we study the effect of the gates on an initialized nuclear spin state, as a function of the number of electron spin pulses in the gate. Figures 2e and 2f of the main text give the Y -projections for both gates for nuclear spin 1. Figure 11 gives the complete set of measurements, including the gates for nuclear spin 2 and the Z -projections that confirm that the gates are conditional and unconditional rotations around X .

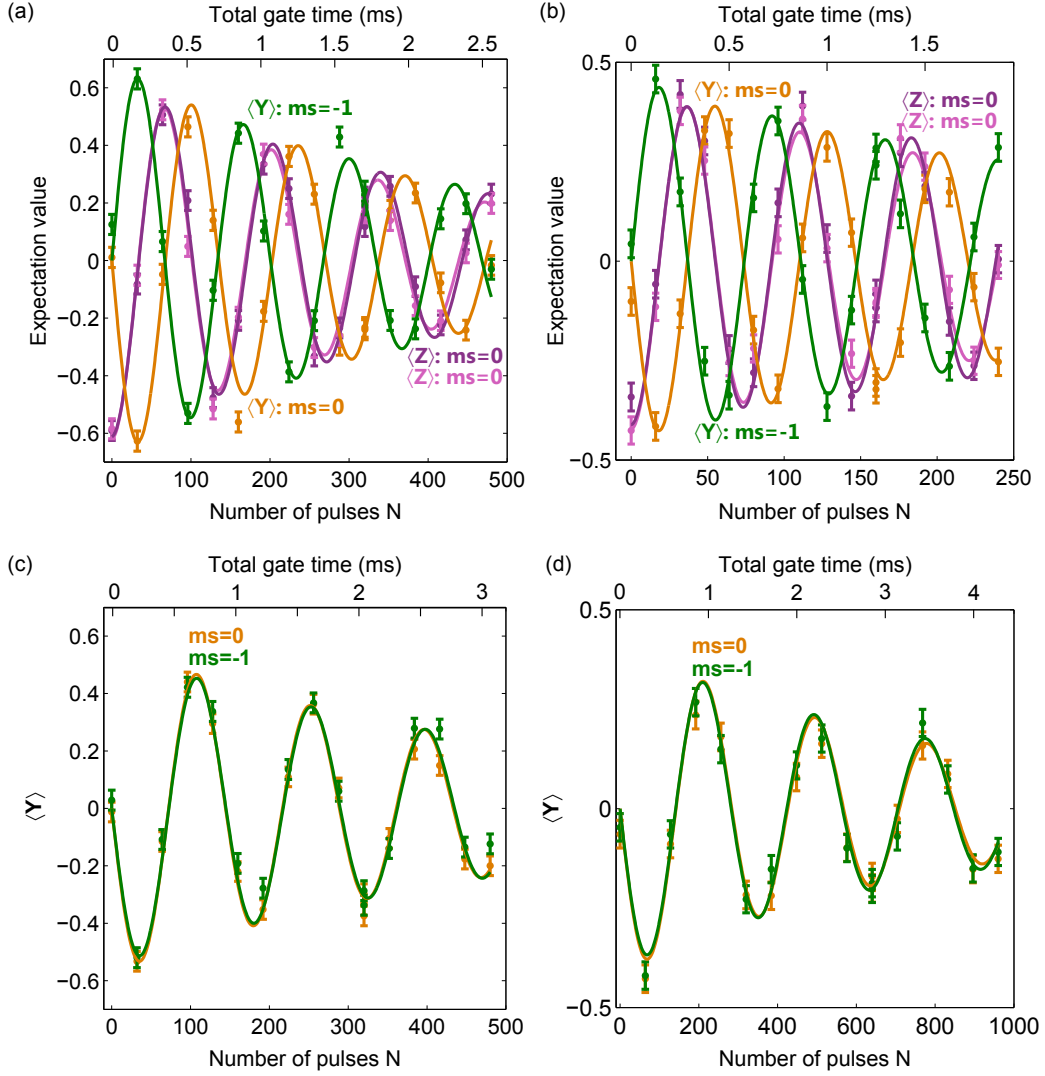


Figure 11: Gate characterization. Action of the conditional (a-b) and unconditional (c-d) gates for both nuclear spin 1 (a-c) and nuclear spin 2 (b-d). Measurement schemes in figure 2e and 2f of the main text. The Z-projection shows that the spin undergoes a Rabi oscillation and the Y-projection shows that the orientation of the rotation is either conditional (a-b) or unconditional on the electron state (c-d). Not corrected for initialization or readout fidelities.

Theoretical gate fidelities

We calculate the theoretical fidelities for the action of the gates on input state $|0\rangle$ (Table III). The results are separated in 3 parts. The first column shows the theoretical fidelity directly as obtained from \hat{V}_0 and \hat{V}_1 . The second column takes into account that the third nuclear spin has a parallel component of the hyperfine interaction A_{\parallel} that differs by less than 10 kHz from nuclear spin 2. This affects the conditional rotation for nuclear spin 2, because the electron spin also entangles slightly with nuclear spin 3. The third column additionally includes the effect of the discretization of τ (experimental resolution of 2 ns). Note that the Z gates are not significantly affected by this because they do not rely on sharp resonances. These fidelities do not take into account the rest of the spin bath or phonon-induced decoherence or depolarization.

NUCLEAR INITIALIZATION FIDELITY

The nuclear initialization fidelity is determined from Ramsey-type experiments as described in the main text. The measurements in Figure 1f and g of the main text are post selected on small magnetic field drifts so that the absolute

	Fidelity	+ Spin 3	+ Discretization precision
Spin 1: $R_X^e(\pm\pi/2)$	0.996		0.987
$R_X(\pi/2)$	0.997		0.993
$R_Z(\pi/2)$	0.999		0.999
Spin 2: $R_X^e(\pm\pi/2)$	0.997	0.959	0.953
$R_Z(\pi/2)$	0.999		0.999

Table III: Theoretical fidelities for the gates. The state fidelity with the target state after applying the gate on $|0\rangle$ and tracing out the electron state. Conditional X -rotation: $R_X^e(\pm\pi/2)$. Unconditional X - and Z -rotations: $R_X(\pi/2)$ and $R_Z(\pi/2)$.

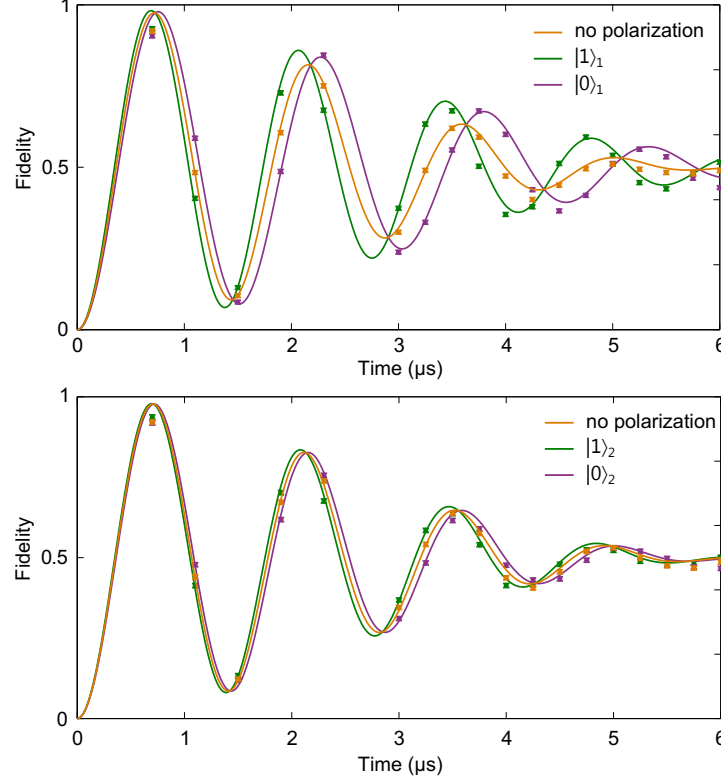


Figure 12: Data set for the determination of the nuclear spin initialization fidelity. Electron spin free evolution measurements with and without nuclear spin initialization. Top: nuclear spin 1, fidelity $F_1 = 0.91(2)$. Bottom nuclear spin 2, fidelity $F_2 = 0.88(5)$. The three curves are measured in a single experiment that is long enough to average over the magnetic field fluctuations, reducing T_2^* to $3.1(1) \mu s$.

increase of T_2^* can be determined. For the initialization fidelity we use an average over a larger data set (Fig. 12). This approach has the advantage that the initialization fidelity can be more accurately determined, but is not suited for measurements of the absolute increase of T_2^* , due to significant magnetic field fluctuations over the extended measurement time. We find $F_1 = 0.91(2)$ for nuclear spin 1 and $F_2 = 0.88(5)$ for nuclear spin 2.

Although the initialization protocol ideally needs only a single application, figure 13 shows that repeated applications do further increase the polarization before saturating after approximately 2 steps. In the implementation of the quantum error correction protocol (Fig. 4 of the main text) only a single initialization step was used so that the initialization fidelities are lower than those obtained from figure 12. The results in figure 13 yield an initialization fidelity for these experiments of $F_1 \approx F_2 \approx 0.82$.

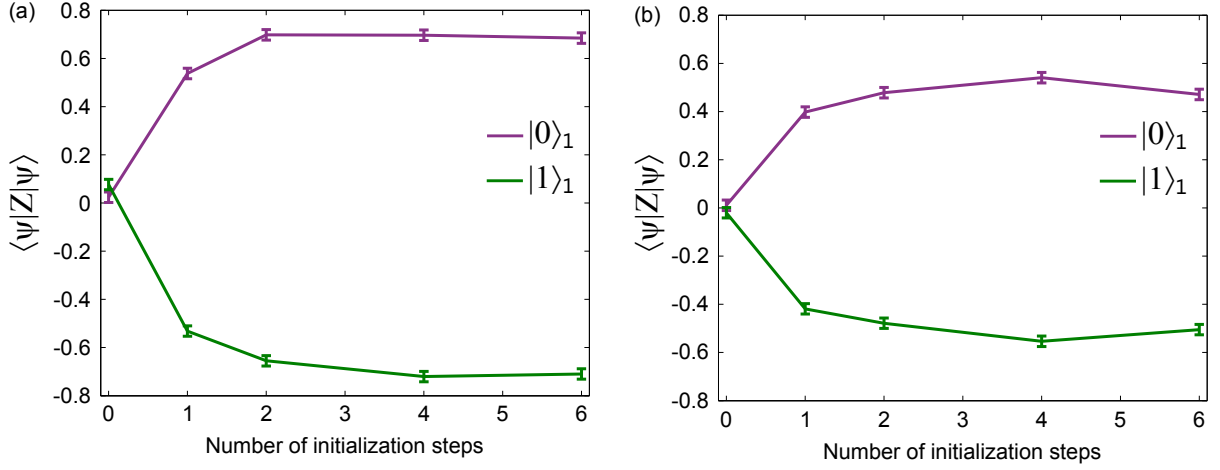


Figure 13: Increased initialization fidelity through multiple initialization steps. The measured expectation value $\langle Z \rangle = \langle \psi | Z | \psi \rangle$ for the nuclear spin state $|\psi\rangle$ as a function of the number of initialization steps. The nuclear spin is either initialized on $|0\rangle$ or $|1\rangle$. (a) Nuclear spin 1. (b) Nuclear spin 2. Data not corrected for initialization or readout fidelities.

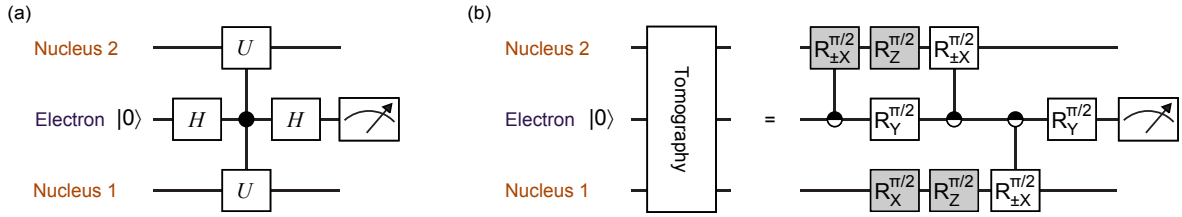


Figure 14: Two-qubit tomography. We measure the expectation values of the different combinations of the nuclear two-qubit pauli operators using the electron spin. (a) General readout scheme to measure $\langle UU \rangle$, with U a unitary operator and H the Hadamard gate. (b) Our implementation. The shaded gates are optional basis rotations.

TWO-QUBIT TOMOGRAPHY

Two-qubit tomography (main text figure 3) is performed by mapping two-qubit correlations onto the electron spin before reading out the electron. Figure 14a shows the general principle and figure 14b shows our implementation.

QUANTUM ERROR CORRECTION

This section discusses the application and characterization of the errors, gives the derivation of the theoretical analysis used in the main text, and gives the complete set of state fidelity results used to derive the process fidelities in the main text (main text Figure 4).

Error implementation

The quantum error correction scheme corrects both coherent errors of the type $R_X(\theta)$, i.e. a rotation around X by angle θ or the quantum map:

$$\epsilon_c(\rho, \theta) = [\cos(\theta/2)I + i\sin(\theta/2)X]\rho[\cos(\theta/2)I - i\sin(\theta/2)X] \quad (17)$$

and non-unitary, decoherence-type, operations given by the quantum map:

$$\epsilon_d(\rho, \theta) = \cos^2(\theta/2)I\rho I + \sin^2(\theta/2)X\rho X \quad (18)$$

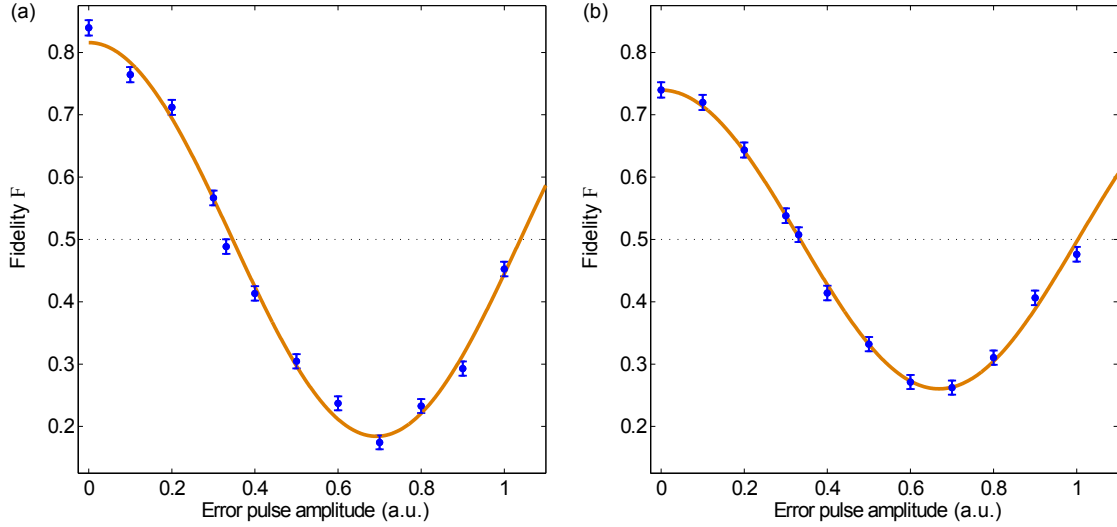


Figure 15: Characterization of the nuclear spin errors. Fidelity F of the final nuclear state with $|Z\rangle = |0\rangle$ as a function of the amplitude of the error pulse applied on the electron. (a) For nuclear spin 1 and (b) for nuclear 2. Lines are fits to the expected cosine behavior around fidelity 0.5. The measurements are not corrected for readout or initialization fidelities.

Errors on the electron spin are directly created by a microwave pulse that implements $R_X(\theta)$. In half the experiments a positive rotation $R_X(+\theta)$ is applied and in the other half a negative rotation $R_X(-\theta)$. The final result is the average over the two measurements, so that the implemented error is of the form of equation 18.

Errors on the nuclear spins are implemented through the electron spin. First the error is applied to the electron spin. Then the initialization gate transfers the error to the nuclear spin state. This operation gives the same result as applying $\epsilon_d(\rho, \theta)$ on an initialized nuclear spin state. Figure 15 shows the resulting fidelity with $|Z\rangle = |0\rangle$ for both nuclear spins as a function of the error pulse amplitude. The observed oscillation around $F = 1/2$ confirms the expected application of the error.

Theoretical analysis

We analyze the quantum error process as a combination of imperfect majority voting and a general decoherence/depolarization process. We assume the following two properties: (1) that applied errors have no effect on the $|\pm X\rangle$ states and (2) that the probabilities that the error correction (majority voting) is successful if qubit 1, qubit 2 or qubit 3 is different from the other two qubits are given by the three p_1 , p_2 and p_3 respectively. These probabilities then completely describe the effectiveness of the error correction process (for an ideal case $p_1 = p_2 = p_3 = 1$).

In each experiment we prepare 6 input states $|\alpha\rangle$:

$$|Z\rangle = |0\rangle, \quad (19)$$

$$|-Z\rangle = |1\rangle, \quad (20)$$

$$|X\rangle = \frac{1}{\sqrt{2}}(|0\rangle + |1\rangle), \quad (21)$$

$$|-X\rangle = \frac{1}{\sqrt{2}}(|0\rangle - |1\rangle), \quad (22)$$

$$|Y\rangle = \frac{1}{\sqrt{2}}(|0\rangle + i|1\rangle), \quad (23)$$

$$|-Y\rangle = \frac{1}{\sqrt{2}}(|0\rangle - i|1\rangle), \quad (24)$$

and measure the expectation values:

$$C_\alpha = \langle \psi_\alpha | \alpha | \psi_\alpha \rangle, \quad (25)$$

where $|\psi_\alpha\rangle$ is the output state for input state $|\alpha\rangle$, and $\alpha = Z, -Z, Y, -Y, X, \text{ or } -X$. The fidelities of the output states with the input states are given by:

$$F_\alpha = C_\alpha/2 + 1/2. \quad (26)$$

We label the 8 possible combinations of (applied) errors that can occur with j . For example: $j = 000$ implies no error, $j = 100$ is an error on Qubit 1, etc. The obtained signal for error combination j and input state $|\alpha\rangle$ is C_α^j . Using the above assumptions all possible results can be described by the probabilities p_1, p_2 and p_3 together with the obtained signals when no error is applied $C_{\pm Z}^{000}$, $C_{\pm Y}^{000}$ and $C_{\pm X}^{000}$. All values based on the above error correction model are given in Table IV.

Signal for error j	$ \pm Z\rangle$	$ \pm Y\rangle$	$ \pm X\rangle$
C_α^{000}	$C_{\pm Z}^{000}$	$C_{\pm Y}^{000}$	$C_{\pm X}^{000}$
C_α^{001}	$(2p_3 - 1)C_{\pm Z}^{000}$	$(2p_3 - 1)C_{\pm Y}^{000}$	$C_{\pm X}^{000}$
C_α^{010}	$(2p_2 - 1)C_{\pm Z}^{000}$	$(2p_2 - 1)C_{\pm Y}^{000}$	$C_{\pm X}^{000}$
C_α^{100}	$(2p_1 - 1)C_{\pm Z}^{000}$	$(2p_1 - 1)C_{\pm Y}^{000}$	$C_{\pm X}^{000}$
C_α^{011}	$-(2p_1 - 1)C_{\pm Z}^{000}$	$-(2p_1 - 1)C_{\pm Y}^{000}$	$C_{\pm X}^{000}$
C_α^{101}	$-(2p_2 - 1)C_{\pm Z}^{000}$	$-(2p_2 - 1)C_{\pm Y}^{000}$	$C_{\pm X}^{000}$
C_α^{110}	$-(2p_3 - 1)C_{\pm Z}^{000}$	$-(2p_3 - 1)C_{\pm Y}^{000}$	$C_{\pm X}^{000}$
C_α^{111}	$-C_{\pm Z}^{000}$	$-C_{\pm Y}^{000}$	$C_{\pm X}^{000}$

Table IV: Action of the error correction protocol. C_α^j is the signal obtained for input state $|\alpha\rangle$ and error combination j . p_n is the probability that an error on qubit n is successfully corrected.

Single-qubit errors

For a variable strength error on one of the qubits the final fidelity for inputs $|\pm Y\rangle$ and $|\pm Z\rangle$ is given by a weighted sum of the two corresponding values in table IV:

$$F_\alpha(\theta) = \frac{\cos^2(\theta/2)}{2} C_\alpha^{klm} + \frac{\sin^2(\theta/2)}{2} C_\alpha^{k'l'm'} + 1/2, \quad (27)$$

in which klm and $k'l'm'$ identify the applied error combination. For example, for the variable error applied to qubit 2 and no error to qubits 1 and 3, we have $klm = 000$ and $k'l'm' = 010$. For $|\pm X\rangle$ the signal is simply constant:

$$F_{\pm X}(\theta) = C_{\pm X}^{000}/2 + 1/2. \quad (28)$$

In figure 4d of the main text two different types of errors are applied: (1) just a variable error on qubit n and (2) a variable error on qubit 2 and a full flip on qubit 1. For a variable error on Qubit n ($n = 1, 2, 3$) and input $|\pm Y\rangle$ or $|\pm Z\rangle$ equation 27 simplifies to:

$$F_\alpha(\theta) = \frac{C_\alpha^{000}}{2} (p_n + (1 - p_n) \cos(\theta)) + 1/2, \quad (29)$$

in agreement with the interpretation of the values p_n as the probability that an error on qubit n is successfully corrected. For the variable error on qubit 2 and a full flip on qubit 1 we find:

$$F_\alpha(\theta) = \frac{C_\alpha^{000}}{2} (p_1 - p_3 + (p_1 + p_3 - 1) \cos(\theta)) + 1/2, \quad (30)$$

which is of the same form as equation 29 and shows that for $p_1 = p_3$ a cosine around fidelity 1/2 is obtained; the error correction is effectively switched of.

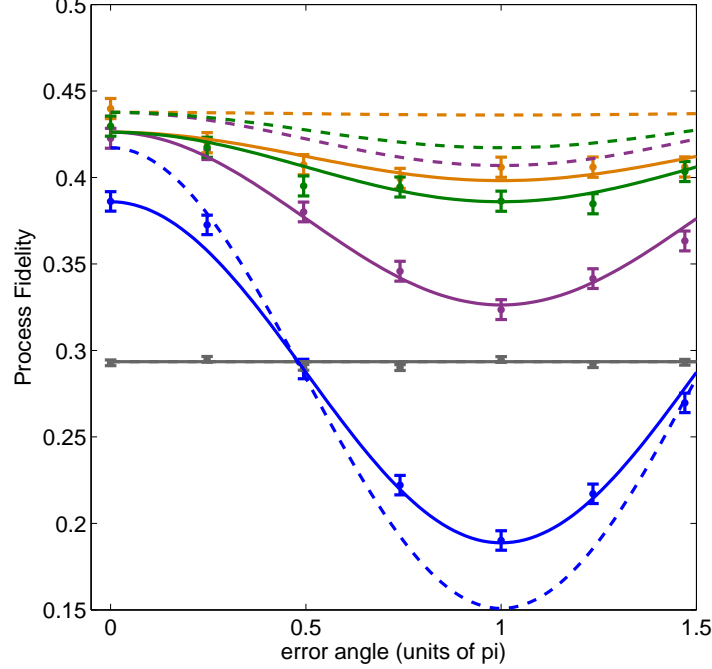


Figure 16: Effect of initialization on the error correction. Process fidelity for selectively applied errors with error angle θ as in figure 4d of the main text. Solid lines are a fit to the model including equation 33. The dashed lines are the expected results for ideal initialization of the two nuclear ancillas ($F_1 = F_2 = 1$).

The process fidelity F_p of the error correction process with the identity is:

$$F_p(\theta) = \frac{F_Z(\theta) + F_{-Z}(\theta) + F_X(\theta) + F_{-X}(\theta) + F_Y(\theta) + F_{-Y}(\theta)}{4} - 1/2, \quad (31)$$

in which the F_α are given by equations 27 and 28. For a single applied error this simplifies to:

$$F_p(\theta) = F_{p0} + A_{YZ}(p_n + (1 - p_n) \cos(\theta)), \quad (32)$$

in which $F_{p0} = (F_X + F_{-X})/4$ and $A_{YZ} = (F_Y(0) + F_{-Y}(0) + F_Z(0) + F_{-Z}(0) - 2)/4$. Note that all the different fidelities without error get grouped into two constants, one related to the average fidelity of the $|\pm X\rangle$ states and one related to the average fidelity of the $|\pm Y\rangle$ and $|\pm Z\rangle$ states without applied errors.

Ancilla initialization fidelity

The above model can be modified to explicitly take the effect of imperfect initialization/polarization of the ancilla qubits (qubit 1 and 3) into account. The effect of the initialization fidelities F_1 and F_2 of the two ancilla qubits is that the measured values C'_α are now combinations of the C_α values in Table IV following:

$$\begin{bmatrix} C'_\alpha{}^{0k0} \\ C'_\alpha{}^{0k1} \\ C'_\alpha{}^{1k0} \\ C'_\alpha{}^{1k1} \end{bmatrix} = \begin{bmatrix} F_1 F_2 & F_1(1 - F_2) & (1 - F_1)F_2 & (1 - F_1)(1 - F_2) \\ F_1(1 - F_2) & F_1 F_2 & (1 - F_1)(1 - F_2) & (1 - F_1)F_2 \\ (1 - F_1)F_2 & (1 - F_1)(1 - F_2) & F_1 F_2 & F_1(1 - F_2) \\ (1 - F_1)(1 - F_2) & (1 - F_1)F_2 & F_1(1 - F_2) & F_1 F_2 \end{bmatrix} \begin{bmatrix} C_\alpha{}^{0k0} \\ C_\alpha{}^{0k1} \\ C_\alpha{}^{1k0} \\ C_\alpha{}^{1k1} \end{bmatrix} \quad (33)$$

This extended model separates the initialization imperfections from imperfections in the error correction process. We take $F_1 = F_2 = 0.82$ as an estimate for the initialization fidelities (Fig. 13). The resulting fits are shown in

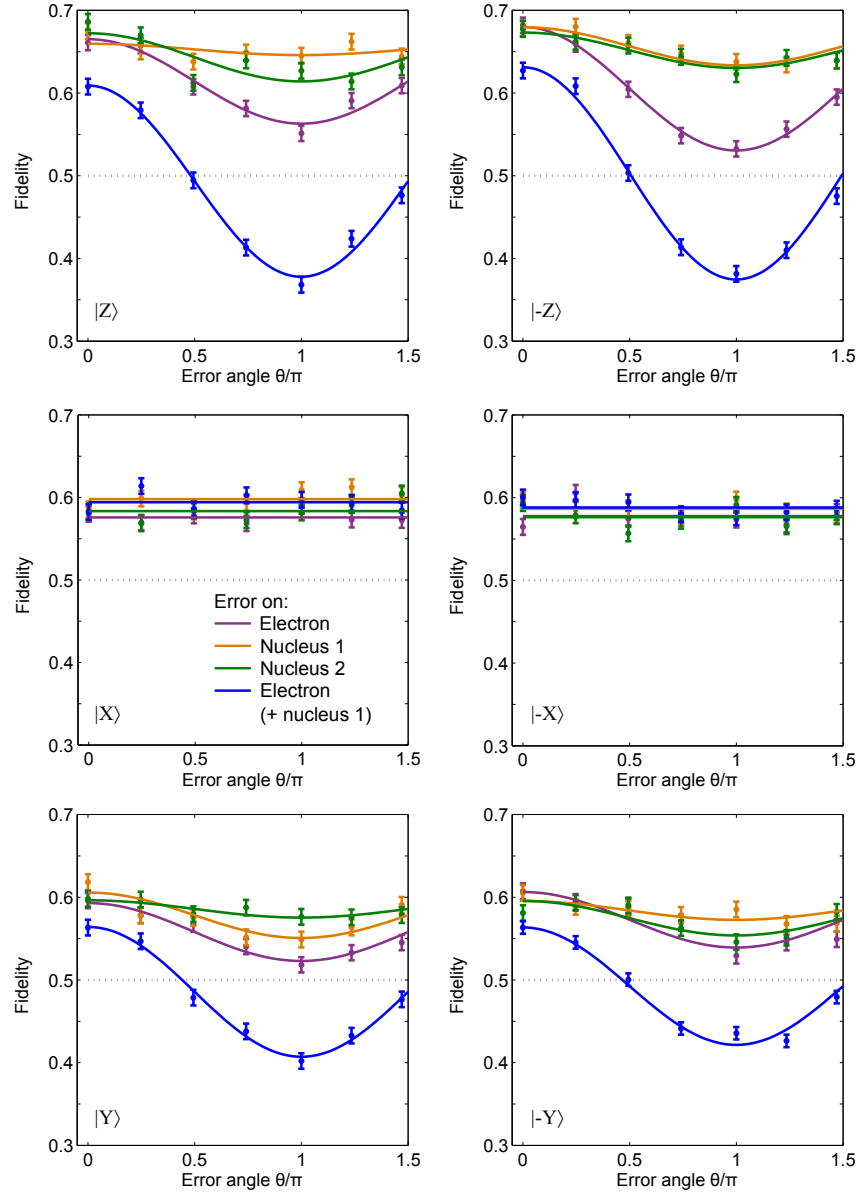


Figure 17: Complete set of state fidelities for selectively applied errors. State fidelity for the 6 input states $|Z\rangle, |-Z\rangle, |X\rangle, |-X\rangle, |Y\rangle$ and $|-Y\rangle$, for 4 different combinations of errors and as a function of the error angle θ . We apply $\epsilon_d(\rho, \theta)$ to each of the three qubits separately and a combination of $\epsilon_d(\rho, \theta)$ to the electron and $\epsilon_d(\rho, \pi)$ to Nucleus 1. Lines are fits to equations 28-30.

figure 16 (solid lines) and yield $p_n = 0.93(3), 0.89(3), 0.99(3)$ and $\langle p_n \rangle = (p_1 + p_2 + p_3)/3 = 0.94(2)$. We calculate the expected result for ideal initialization by using the same value for p but now setting $F_1 = F_2 = 1$ (dashed lines, Fig. 16). The imperfect initialization has two effects. First it strongly affects the success probability of the error correction as double errors (one initialization error + one applied error) cannot be corrected. Second, it lowers the overall maximum fidelity. This is a weak effect because it requires an error in the preparation of both ancillas at the same time and is therefore proportional to $(1 - F_1)(1 - F_2)$.

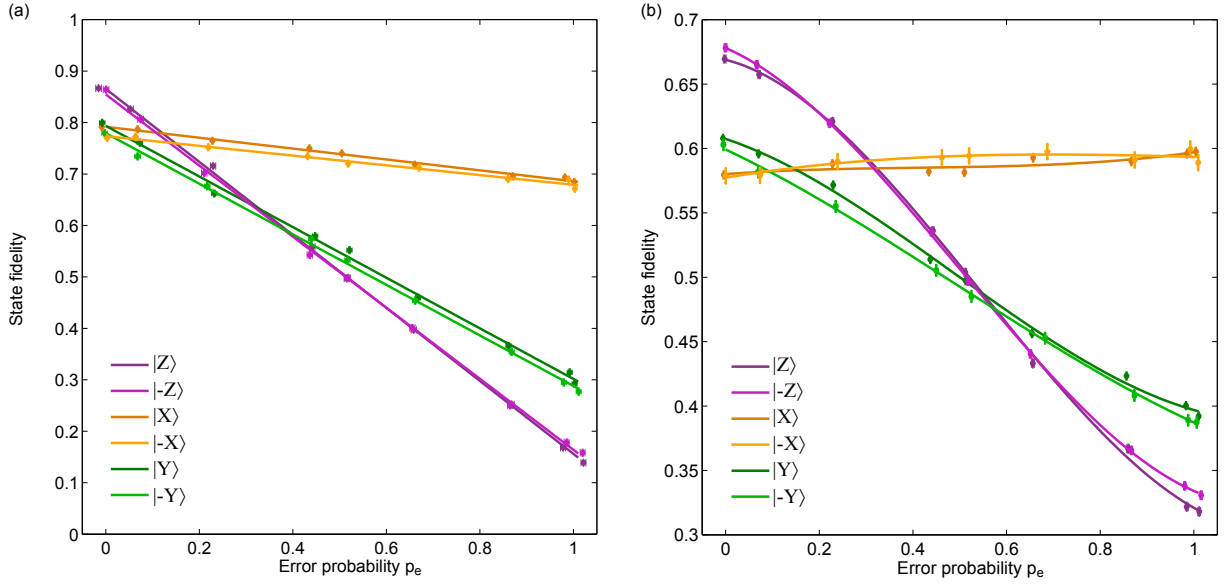


Figure 18: (a) State fidelities for the 6 input states as a function of the error probability without error correction. Lines are linear fits to the data. (b) State fidelities for the 6 input states as a function of the error probability with error correction. Lines are 3^{rd} order polynomial fits to the data.

Simultaneous errors

The process fidelity F_p for simultaneous errors is given by:

$$F_p(p_e) = (1 - 3p_e + 3p_e^2 - p_e^3)F_p^{000} \quad (34)$$

$$+ p_e(1 - p_e)^2(F_p^{001} + F_p^{010} + F_p^{100}) \quad (35)$$

$$+ p_e^2(1 - p_e)(F_p^{011} + F_p^{101} + F_p^{110}) \quad (36)$$

$$+ p_e^3 F_p^{111}, \quad (37)$$

with $p_e = \sin(\theta/2)^2$ the error probability and F_p^{klm} the process fidelity for applied error klm , i.e.:

$$F_p^{klm} = 1/4 \left(1 + \frac{C_X^{klm} + C_{-X}^{klm}}{2} + \frac{C_Y^{klm} + C_{-Y}^{klm}}{2} + \frac{C_Z^{klm} + C_{-Z}^{klm}}{2} \right). \quad (38)$$

with C_α^{klm} as given in Table IV we obtain:

$$F_p(p_e) = F_{p0} + A_{YZ} [1 - 3p_e + 3p_e^2 - 2p_e^3 + 3(2\langle p_n \rangle - 1)(p_e - 3p_e^2 + 2p_e^3)], \quad (39)$$

The experiment is completely described by just 3 parameters: the offset F_{p0} (due to the average $|\pm X\rangle$ fidelity without applied errors), the amplitude A_{YZ} (due to the average $|\pm Y, Z\rangle$ fidelity without applied errors) and the average error correction probability $\langle p_n \rangle$.

Complete state fidelity data set

The complete set of state fidelities used to derive the process fidelities for errors applied to one of the qubits at a time (main text figure 4d) is shown in figure 17. The complete sets of state fidelities used to obtain the process fidelities for simultaneously applied errors (Fig. 4e of the main text) are given in figure 18a (without error correction) and figure 18b (with error correction).

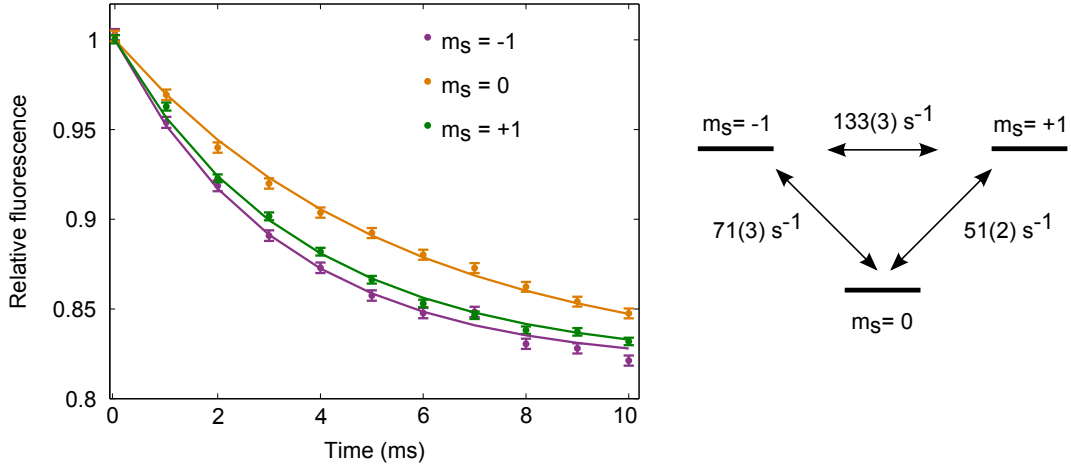


Figure 19: Electron depolarization data and fit to three-level model. The fluorescence of the final electron readout is shown relative to the fluorescence for $m_s = 0$ preparation. The fits additionally use the measured fluorescence for $m_s = -1$ and $m_s = +1$ preparation.

DECOHERENCE AND DEPOLARIZATION

In this section we analyze the different decoherence mechanisms in the three-qubit register.

Electron depolarization “ T_1 ”

The electronic depolarization (longitudinal relaxation or T_1 -type process) due to phonon interactions plays an important role at these room temperature experiments. To measure the depolarization rates we prepare one of the three states $m_s = -1$, $m_s = 0$ and $m_s = +1$ and let the system relax for a time t . We then apply a pi-pulse on the $m_s = 0$ transition (for the state starting in $m_s = 0$ nothing is done) before reading out the electron. The results are fit to a 3-level model that yields three rates between the different levels (Fig. 19). We find: $\Gamma_{0,-1} = 71(3) \text{ s}^{-1}$, $\Gamma_{0,+1} = 51(2) \text{ s}^{-1}$ and $\Gamma_{-1,+1} = 133(3) \text{ s}^{-1}$. In this three level system no unique “ T_1 ” value can be defined. Nevertheless, a separate analysis of each of the curves gives $1/e$ times of $3.24(9) \text{ ms}$ ($m_s = -1$), $5.11(7) \text{ ms}$ ($m_s = 0$, which is often reported as the T_1 value) and $3.91(6) \text{ ms}$ ($m_s = +1$). We verified that the same rates were obtained with a 4 times lower laser output power, indicating that transitions induced by background illumination are negligible.

Electron decoherence T_{coh}

To measure the electronic coherence time under dynamical decoupling T_{coh} the electron spin is prepared along X . We then apply a decoupling sequence with $\tau = 2\pi/\omega_L = 2.324 \mu\text{s}$ and measure the spin projection along X . The total time is varied by varying the number of pulses N in the sequence. The result is shown in figure 20.

The green line marks the limit given by phonon-induced depolarization of the electron spin. It is given by the total decay rate out of the $m_s = 0$ and $m_s = -1$ levels: $\Gamma_{0,-1} + \Gamma_{0,+1}/2 + \Gamma_{-1,+1}/2$. The additional decoherence observed experimentally is consistent with previous reports [6] and is likely due to phonon-induced dephasing, as much longer coherence times were reported at low temperatures [6, 7]. The expected signal without phonon-induced dephasing and depolarization is given by:

$$S = e^{-\left(\frac{2\tau}{T_2}\right)^n N}, \quad (40)$$

with the spin echo time $T_2 = 251(7)\mu\text{s}$. With $n = 3$ this gives an estimated decay time of $\sim 700 \text{ ms}$, indicating that decoupling from the spin bath is not the limiting factor.

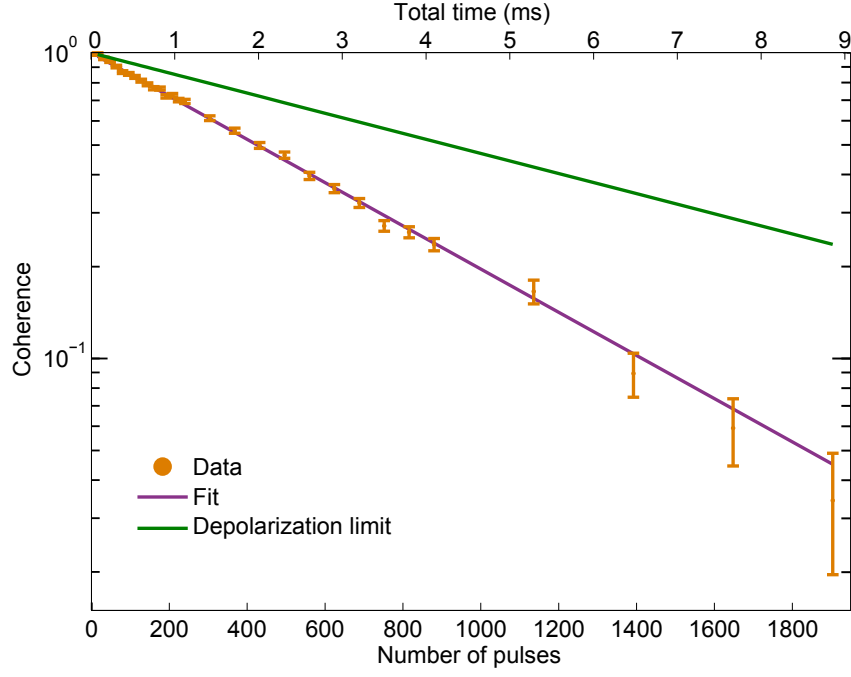


Figure 20: Decoherence of the electron spin under dynamical decoupling. We apply a decoupling sequence to input state $|X\rangle$ and measure the final state along X . The interpulse delay τ is $2\pi/\omega_L$, in the same range as used for the nuclear gates. Purple: Exponential fit to the data that gives $T_{coh} = 2.86(4)$. Green: expected value due to electron depolarization alone.

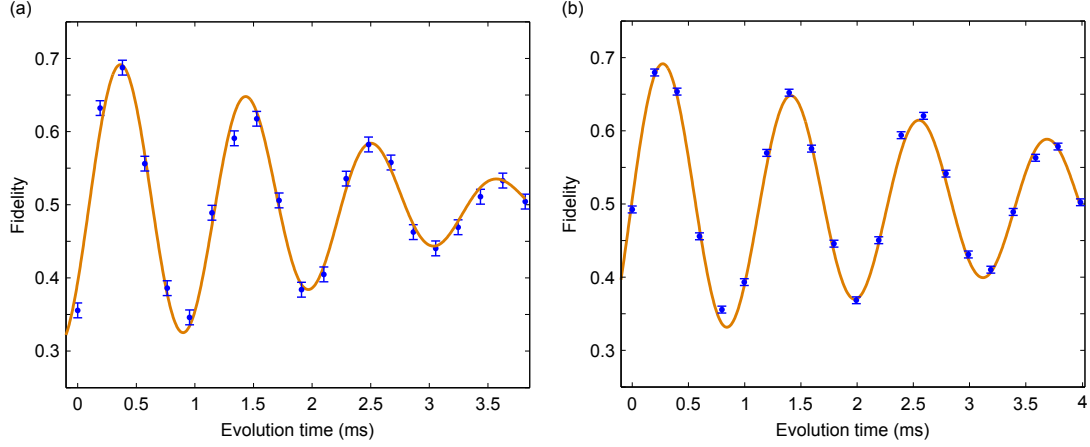


Figure 21: Nuclear dephasing time T_2^* . (a) For nuclear spin 1. $T_2^* = 2.7(2)$ ms, simultaneously measured electron $T_2^* = 3.4(1)\mu s$. (b) For nuclear spin 2. $T_2^* = 4.4(5)$ ms, simultaneously measured electron $T_2^* = 3.18(8)\mu s$. Fits are sine functions with a decaying envelope $e^{(-t/T_2^*)^\delta}$. Spin 1: $\delta = 2$, spin 2: $\delta = 1$. No readout correction.

Nuclear dephasing T_2^*

We measure the nuclear dephasing time T_2^* by preparing the nuclear spin in a superposition and the electron spin in $m_s = 0$, and let the system evolve for variable time. The electron spin is then reset to $m_s = 0$ before the nuclear spin is measured along an axis that creates an effective detuning of approximately 1 kHz. We obtain $T_2^* = 2.7(2)$ ms for nuclear spin 1 and $T_2^* = 4.4(5)$ ms for nuclear spin 2 (Fig. 21). An electron free-precession (Ramsey-type) measurement is performed during the experiments (interleaved on a μs timescale), so that the electron and nuclear T_2^* can be compared under the same magnetic field fluctuations.

We expect the nuclear dephasing time to be set by a combination of electron relaxation and magnetic field fluctua-

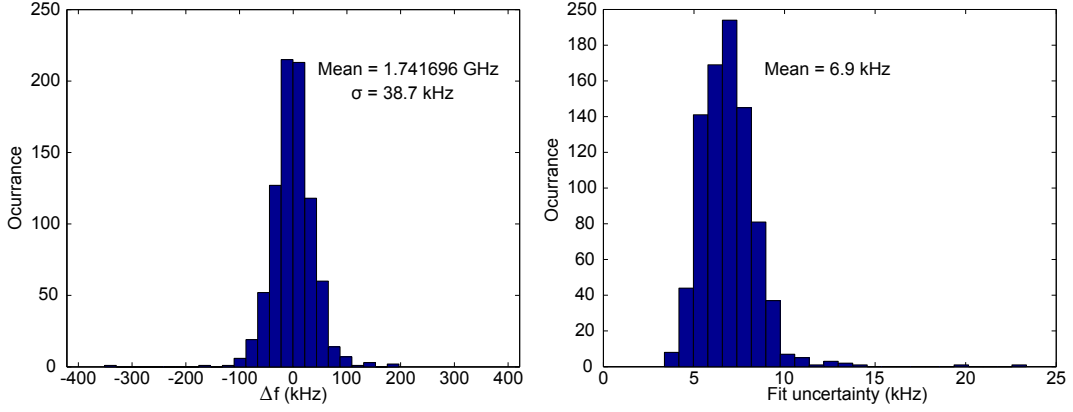


Figure 22: Magnetic field stabilization. The magnetic field during the error correction measurements was stabilized by a feedback loop based on 840 measurements. (left) Electron energy splitting. Fluctuations during the experiment of 38.7 kHz (1σ) are observed, corresponding to 14 mG. (right) The average measurement uncertainty in a single instance of the magnetic field measurement is 6.9 kHz (2 mG).

tions (including the nuclear spin bath). Electron relaxation gives a rate of $\Gamma_{0,-1} + \Gamma_{0,+1} = 122(4) \text{ s}^{-1}$ (time constant of 8.2 ms). To estimate the intrinsic nuclear dephasing timescale T_{2int}^* we subtract the electron depolarization rate from the inverse of the measured dephasing time T_2^* . We find $T_{2int}^* \sim 4.0$ ms for spin 1 and $T_{2int}^* \sim 9.5$ ms for spin 2. The difference in these values could originate from the differences in the nuclear spin's microscopic environments.

Magnetic field stability

We stabilize the magnetic field through a feedback loop by periodically measuring the energy splitting of the NV centre. This stabilization is required to counteract slow magnetic field drifts (order of 0.1 G) over the measurement time. Figure 22 characterizes the magnetic field stability during the quantum-error-correction measurements with simultaneous errors (taken over a total of 344 hours, spread out over 1 month). These values are representative for the other measurements.

The measured residual slow fluctuations of the magnetic field (38.7 kHz, 0.014 G) are small compared to the fast fluctuations due to the ^{13}C bath (~ 66 kHz, 0.024 G). These slow fluctuations are expected to decrease the electron T_{2e}^* from the instantaneous value $3.3 \mu\text{s}$ to $2.9 \mu\text{s}$ (and the nuclear T_2^* with approximately the same factor).

Part of the fluctuations are caused by the uncertainty in the measurements of the electron splitting. Figure 22 shows that this effect is small, because the measurement uncertainty of (6.9 kHz) is small compared to the total drift observed (38.7 kHz).

Nuclear T_2

The nuclear spin coherence times can be extended by decoupling from the spin bath. Figure 23 shows the results of nuclear spin echo experiments. The required pi-pulse is constructed in the same way as all nuclear gates in this work. The electron is prepared in $m_s = 0$ and re-initialized before the pi-pulse, which makes it possible to use a conditional gate, and re-initialized again to be used in the final measurement. We find $T_2 = 5.9(8)$ ms (nuclear spin 1) and $T_2 = 9(1)$ ms (nuclear spin 2).

Nuclear dephasing T_2^* and depolarization T_1 under laser illumination

Being able to re-initialize the electron spin without depolarizing or dephasing the nuclear spins is essential for initializing the multiqubit register and for performing partial measurements within such registers.

Figure 24 shows a T_2^* under illumination of $51(7) \mu\text{s}$ for nuclear spin 1 and $0.35(9)$ ms for nuclear spin 2. These times are long compared to the time required to re-initialize the electron spin ($\sim 2 \mu\text{s}$). For example, for nuclear spin 1 this predicts a contrast loss of approximately $1 - e^{-2/50} = 0.04$.

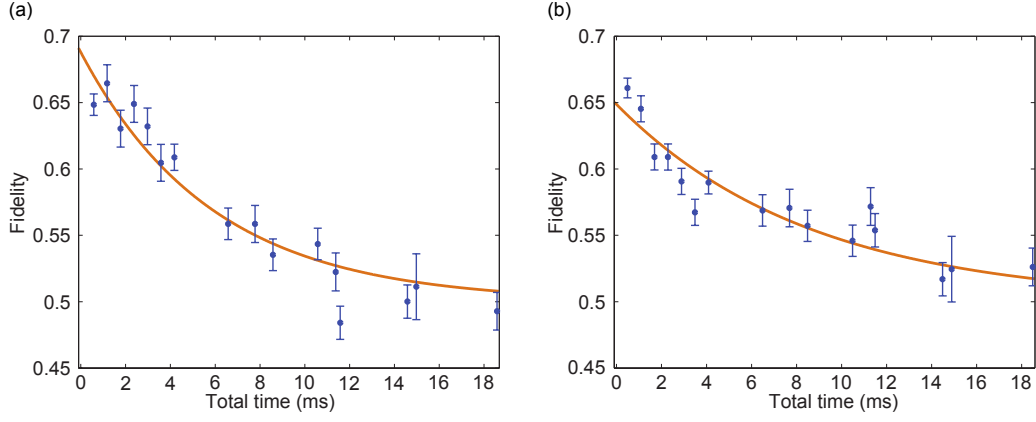


Figure 23: Nuclear spin echo experiments. (a) for nuclear spin 1: $T_2 = 5.9(8)$ ms. (b) for nuclear spin 2: $T_2 = 9(1)$ ms. Single exponential fits. No readout or initialization correction.

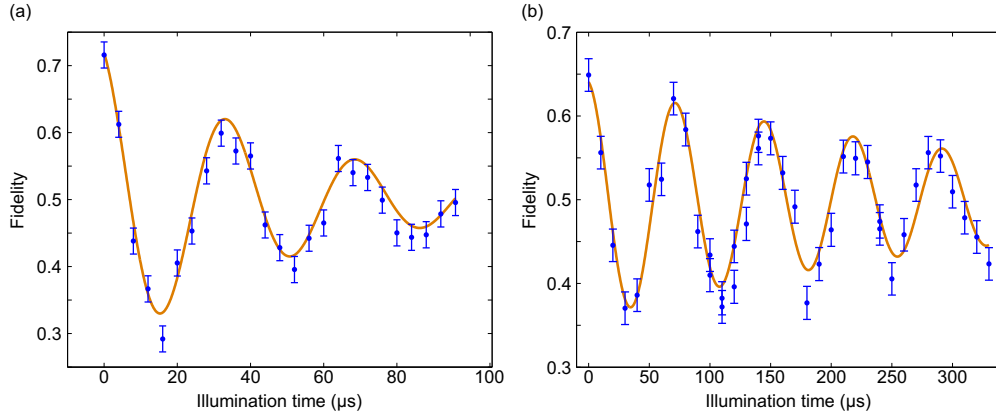


Figure 24: Nuclear Ramseys and T_2^* under illumination. (a) nuclear spin 1, $T_2^* = 51(7)$ μs. (b) nuclear spin 2, $T_2^* = 0.35(9)$ ms. The laser power is the same as used in the initialization, re-initialization and readout steps. No readout or initialization correction.

Figure 25 shows nuclear relaxation measurements for the both spins, with and without laser illumination. The nuclear spin is prepared in $|0\rangle$ and the electron spin in $m_s = 0$. We let the system relax for a variable time during which the laser is either on or off. For the experiment without laser illumination, the electron is reset by a short laser pulse ($2\mu\text{s}$) so that it can be used to measure the nuclear spin state. Without illumination, we find $T_1 = 0.04(1)$ s and $T_1 = 21(5)$ ms for spin 1 and 2 respectively. With illumination, we find $T_1 = 2.5(3)$ ms and $T_1 = 1.2(2)$ ms for spin 1 and 2 respectively.

The nuclear depolarization during laser illumination is slow compared to the time it takes to re-initialize the electron spin ($\sim 2\mu\text{s}$), so that the electron can be re-initialized without depolarizing the nuclei. Note that the final signal approaches a fidelity of 0.5; prolonged laser light does not create a preferential polarization for these nuclear spins.

FIDELITY ESTIMATES

The estimates for the final fidelities for the three-qubit quantum error correction protocol in the main text are obtained from the values above as follows. We take the electron decoherence time ($T_{coh} = 2.86(4)$ ms) and the two nuclear spin intrinsic dephasing times ($T_{2int}^* \sim 4.0$ ms and $T_{2int}^* \sim 9.5$). As a rough estimate we approximate the three processes for the three qubits by rates and add them to obtain a final decay time $T_{est} = 1.4$ ms. The typical fidelity for the 1.8 ms quantum error correction protocol becomes $F_{est} = e^{-1.8/T_{est}}/2 + 1/2 = 0.64$. This corresponds to estimated process fidelity $F_{p,est} = 6F_{est}/4 - 1/2 = 0.46$, similar to the observed value. The average gate fidelity for the 10 nuclear gates in the error correction protocol is estimated from $F_{average} = 1/2 \sqrt[10]{2F_{est} - 1} + 1/2 = 0.94$.

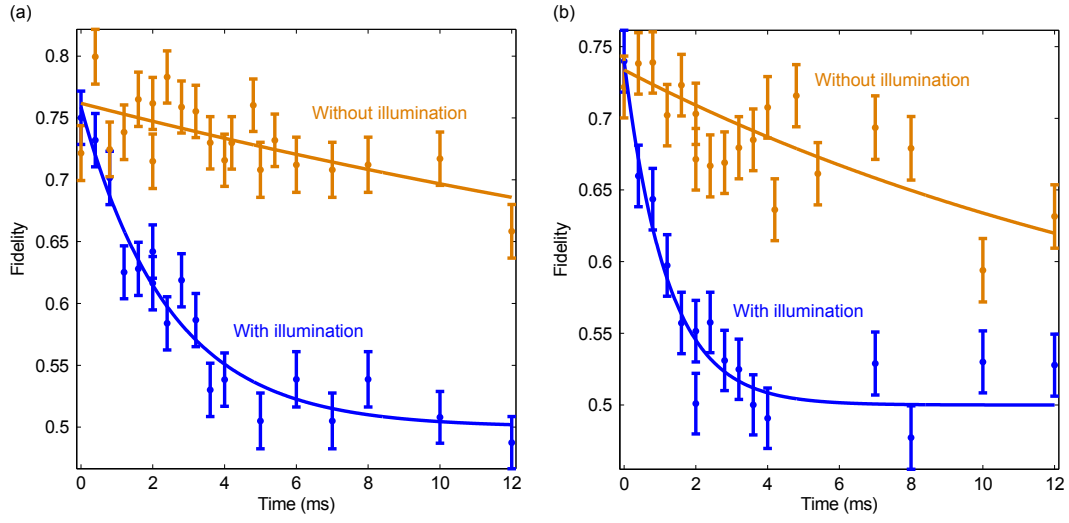


Figure 25: Nuclear T1 with and without illumination. Lines are exponential fits. (a) nuclear spin 1. (b) nuclear spin 2. The laser power is the same as used in the initialization, re-initialization and readout steps. No readout correction.

-
- [1] Van der Sar, T. et al., *Nature* **484**, 82 (2012).
 - [2] Bernien, H. et al., *Phys. Rev. Lett.* **108**, 043604 (2012).
 - [3] Smeltzer, B., McIntyre, J., Childress, L., *Phys. Rev. A* **80** (5), 050302 (2009).
 - [4] Jacques, V. et al., *Phys. Rev. Lett.* **102** (5), 057403 (2009).
 - [5] Taminiau, T.H. et al., *Phys. Rev. Lett.* **109**, 137602 (2012).
 - [6] Bar-Gill, N., Pham, L.M., Jarmola, A., Budker, D., Walsworth, R.L., *Nat. Commun.* **4**, 1743 (2013).
 - [7] Bernien, H. et al., *Nature* **497**, 7447 (2013).
 - [8] Aslam, N., Waldherr, G., Neumann, P., Jelezko, F., Wrachtrup, J., *New J. Phys.* **15**, 013064 (2013).
 - [9] Aslam, N. et al., *Phys. Rev. Lett.* **107**, 090401 (2011).
 - [10] Pfaff, W. et al., *Nature Phys.* **9**, 29 (2013).